



HAL
open science

Functionalization of poly(glycidylmethacrylate) with iminodiacetate and imino phosphonate groups for enhanced sorption of neodymium - sorption performance and molecular modeling

Ahmed Galhoum, Takaya Akashi, Mikko Linnolahti, Janne Hirvi, Abdullah Al-Sehemi, Abul Kalam, Guibal Eric

► To cite this version:

Ahmed Galhoum, Takaya Akashi, Mikko Linnolahti, Janne Hirvi, Abdullah Al-Sehemi, et al.. Functionalization of poly(glycidylmethacrylate) with iminodiacetate and imino phosphonate groups for enhanced sorption of neodymium - sorption performance and molecular modeling. *Reactive and Functional Polymers*, 2022, 180, pp.105389. 10.1016/j.reactfunctpolym.2022.105389 . hal-03773443

HAL Id: hal-03773443

<https://imt-mines-ales.hal.science/hal-03773443v1>

Submitted on 12 Sep 2022

HAL is a multi-disciplinary open access archive for the deposit and dissemination of scientific research documents, whether they are published or not. The documents may come from teaching and research institutions in France or abroad, or from public or private research centers.

L'archive ouverte pluridisciplinaire **HAL**, est destinée au dépôt et à la diffusion de documents scientifiques de niveau recherche, publiés ou non, émanant des établissements d'enseignement et de recherche français ou étrangers, des laboratoires publics ou privés.

Functionalization of poly(glycidylmethacrylate) with iminodiacetate and imino phosphonate groups for enhanced sorption of neodymium - sorption performance and molecular modeling

Ahmed A. Galhoum^{a,b,*}, Takaya Akashi^a, Mikko Linnolahti^c, Janne T. Hirvi^c, Abdullah G. Al-Sehemi^{d,e}, Abul Kalam^{d,e}, Eric Guibal^f

^a Faculty of Bioscience and Applied Chemistry, Hosei University, 3-7-2, Kajino-chou, Koganei, Tokyo 184-8584, Japan

^b Nuclear Materials Authority, P.O. Box 530, El-Maadi, Cairo, Egypt

^c Department of Chemistry, University of Eastern Finland, Joensuu Campus, 80101 Joensuu, Finland

^d Research Center for Advanced Materials Science (RCAMS), King Khalid University, P.O. Box 9004, Abha 61413, Saudi Arabia

^e Department of Chemistry, College of Science, King Khalid University, P.O. Box 9004, Abha 61413, Saudi Arabia

^f Polymers Composites and Hybrids, Institut Mines Telecom – Mines Ales, 6 avenue de Clavières, F-30319 Alès, cedex, France

A B S T R A C T

Polyglycidyl methacrylate (PGMA, obtained by dispersion polymerization method) can be successfully functionalized to improve the sorption of Nd(III). Pristine PGMA is first modified by amination (N-PGMA), before grafting amino-alkylcarboxylate and amino-alkylphosphonic ligands to produce A-PGMA and P-PGMA, respectively. These materials are characterized by CHNP, FTIR-spectrometry, XRD, TG-TDA and pH_{zpc} . Following that, the Nd(III) sorption properties are compared. At optimum pH: 4.5–5.0, the sorbents can be ranked according to the series: P-PGMA ($0.645 \text{ mmol Nd g}^{-1}$) < A-PGMA ($0.736 \text{ mmol Nd g}^{-1}$) (vs. $0.304 \text{ mmol Nd g}^{-1}$ for N-PGMA). Sorption capacities increase with temperature. Sorption isotherms are modeled using the Langmuir equation. Equilibrium is reached within 180 min. Uptake kinetics are controlled by the resistance to intraparticle diffusion (fitted by the Crank equation). The sorption is endothermic, spontaneous and followed by an increase of the entropy of the system. Elution and regeneration are carried out using HNO_3 solutions achieving >91%. Theoretical DFT calculation (molecular modeling) and FTIR spectroscopy, the interactions of Nd(III) with reactive functional groups (carboxyl, hydroxyl, amine and phosphonate groups) are characterized. Finally, the sorbents are tested on pre-treated leachate of Egyptian monazite: REEs' sorption performances are correlated with their intrinsic properties and compared for the two sorbents.

Keywords:

Chemical functionalization of poly(glycidylmethacrylate)
Neodymium
Sorption isotherms and kinetics studies
Metal desorption and regeneration
Molecular modeling

1. Introduction

Rare earths (REEs; yttrium, scandium and lanthanide series) are vital components in the high-tech materials, photovoltaic, magnets, catalysts, metallurgical sectors and developments in nuclear energy [1]. The growing need for these metals and the geographic distribution of these resources made the exploitation of REEs a strategic and geopolitical issue for industry and governmental authorities. More generally, increasing constraints on environmental discharge of hazardous metals in contaminated effluents and the necessity to find new sources for strategic metals have motivated incentive politics for recovering valuable metals from secondary sources such as waste streams, tailings, spent materials, or waste electric and electronic equipment (WEEEs)

[2–6]. In most cases, the recovery of REEs from these secondary resources involves pre-separation techniques (densitometry and magnetic separations) and leaching operations (usually acidic leaching) [7,8]. These enriched leachates may be treated using different techniques depends on the solutions composition (concentration, acidity, competitor ions, salinity, etc.). Among the most familiar processes appear: precipitation, solvent extraction (and associated processes such as extractant-supported and emulsion membranes, impregnated resins) [9–15], ion-exchange resin [16,17], ion-imprinted resin [18] and chelating resins [19–21].

Sorption (Ion-exchange and/or chelating resins) is a promising method for recovering metal ions from dilute effluents, experimenting with their affinity of functional groups [22–25]. Chelating resins/

* Corresponding author at: Faculty of Bioscience and Applied Chemistry, Hosei University, 3-7-2, Kajino-chou, Koganei, Tokyo 184-8584, Japan.
E-mail address: galhoum_nma@yahoo.com (A.A. Galhoum).

sorbents, are *multifunctional* materials which have been intensively explored for metal ion extraction and recovery, as well as water purification. The most often utilized functional group atoms consist of nitrogen (N as in $>NH/-NH_2$, $-N=N-$, $C(=O)NH_2$, $-CN$ groups), oxygen (O in $-COOH$, $-OH$, $-O-$, $>C=O$ groups) [26], phosphorus (in the form of phosphoryl groups, $P=O$ and/or $P-OH$ groups) [27] and sulfur (S as in $-SH$, $RSC(=O)NR_2$, $-S-$ groups) [28,29]. The attached molecules which have O-, N-, P-, and/or S-donor atoms, or a mixture and blend of them, acting as basic centers, enhancing the density of sorption sites and allowing selective extraction [22,30].

Grafting additional types of functional groups can modify the reactivity (e.g. carboxyl groups,

either alone or as a group with amine groups) by inserting amino, phosphonic and carboxylic acid groups [31,32], amino-acids [33] and aminophosphonic acids [34]. Aminophosphonate derivatives have been used in previous research to validate the interest of these reactive groups for uranium and rare earths sorption [20,30], via parallel with solvent extractants and synthetic resins [12].

Glycidyl methacrylate (GMA) is a vinyl-epoxy monomer, that meets the further-polymerization modification criteria via a ring-opening process using various reagents e.g. amines, amino-acids, carboxylic acids, etc. [35,36]. The interest of this support also derives from its low-cost; indeed, it's commonly utilized in the manufacturing of epoxy functional methacrylic resins in the industry (i.e. Coatings and adhesives are commonly used) [36,37].

The polymerization facilities and the reactivity of GMA precursor offer very attractive perspectives for elaborating a wide diversity of functionalized resins; including bi-functionalization. Herein, two bi-functionalized PGMA derivatives have been synthesized through an intermediary step involving the amination of PGMA (N-PGMA). In the next step, N-PGMA was grafted with amino-alkylcarboxylate moieties and amino-alkylphosphonic acid groups to produce iminodiacetate PGMA (A-PGMA) and iminodiphosphonate PGMA (P-PGMA), respectively. The synthesis routes are characterized through different analytical techniques: elemental analysis, FTIR characterization, titration, thermogravimetric analysis. After that, the sorption characteristics of A-PGMA and P-PGMA for Nd(III) are examined and compared: pH, uptake kinetics and sorption isotherms (at various temperatures) are all given considerable consideration. Acidic solutions are tested for metal recovery and sorbent recycling. The last part focuses on the recovery of REEs from Egyptian monazite (with evaluation of the correlation between intrinsic characteristics of REEs and their relative affinities for A-PGMA and P-PGMA).

The characterization by FTIR of the interactions with Nd(III) is completed by a theoretical analysis of the interaction modes using density functional theory calculations. The adsorption energy is minimized to evaluate the most probable mode of interactions; the simulation of electronic cloud distribution helps in selecting the most appropriate bonds.

2. Experimental work

2.1. Chemicals

Glycidyl methacrylate, monochloroacetic acid, ammonia solution (33%), formaldehyde solution (37%) and polyvinylpyrrolidone (PVP K-30) were received from Wako chemical Co. Ltd. (Osaka, Japan). Neodymium(III) chloride ($NdCl_3$) was dissolved in concentrated HCl under warming, then diluted with demineralized H_2O to prepare a stock solution (1 g Nd L^{-1}). Phosphorous acid, 2,2-azobisisobutyronitrile (AIBN) and $NdCl_3$ were delivered by Sigma-Aldrich (Saint-Luis, MI, USA). All other reagents were supplied by Prolabo chemicals (VWR, Avantor Group, Fontenay-sous-Bois, France) and were used obtained.

2.2. Materials synthesis

The synthesis of functionalized sorbents is summarized in [Scheme 1](#) [38]. Step1: the PGMA micro-spheres were synthesized via dispersion polymerization. In a four-necked flask (250 mL) to make the dispersion solution: 3 g of PVP K-30 was dissolved in a 122 mL ethanol/water solution (90% w/w). AIBN initiator (0.2 g) was added to the GMA monomer phase (10 g, or ~ 9.6 mL), before transferring the mixture to the dispersion solution: N_2 was sprayed into the solution for 30 min [35]. The mixture was then refluxed for 24 h at 70°C with mechanical stirring (120 rpm) [35]. The product (i) (i.e., PGMA) was filtered off and repeatedly washed with ultrapure water and ethanol for several times; before being dried under vacuum at room temperature (~ 4.89 g). The fraction 75–100 μm was collected for further modifications.

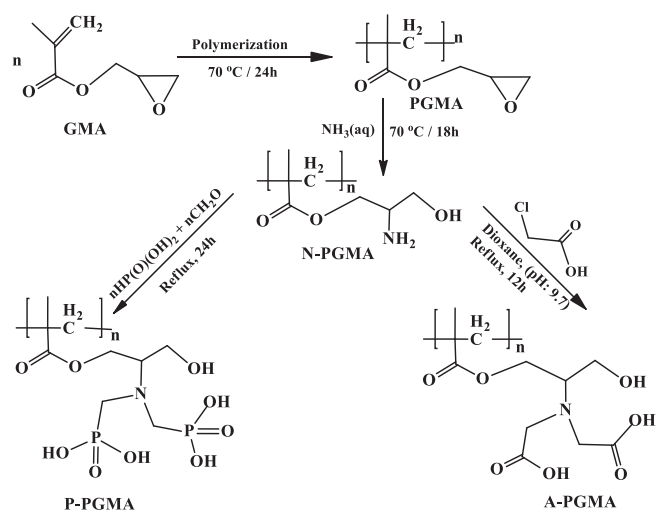
Step 2: In ethanol (20 mL), 2.5 g of PGMA were dispersed, and after that, 30 mL of ammonia was added. Under reflux at 80°C , the suspension was agitated for 18 h [38]: the N-PGMA (product (ii)) was filtrated and washed thoroughly (ethanol and H_2O) (~ 2.75 g, d.w.).

The procedure of phosphonic acid grafting onto N-PGMA was performed as follows: 3 g of phosphorous acid in water/HCl solution (50 mL, (v/v: 1:1) is reacted with N-PGMA (1.32 g) in a three-necked flask. Under reflux, the mixture was heated and 7.5 mL of formaldehyde solution was slowly added in-drops within 60 min. For a further 24 h, the reaction was kept under reflux [38]. To graft carboxylic acid groups: N-PGMA (1.29 g) was suspended in DMF (dimethylformamide, 25 mL), then chloroacetic acid (10 g / 25 mL H_2O , pH 0: 9.57) was added to the suspension. The suspension was agitated under reflux for 18 h, after pH was adjusted to 9.0–9.5 [38]. The final products were filtrated, thoroughly washed (EtOH and H_2O) and dried at 80°C to produce P-PGMA (imino-phosphonate-derived PGMA, ~ 1.75 g, d.w.) and A-PGMA (iminoacetate-derived PGMA) (~ 1.58 g, d.w.). Actual yields of grafting are probably a little higher than documented because of weak losses of materials during separation steps (filtration) and/or gluing (and deposition) onto flasks.

The proposed theoretical mechanisms involved in the synthesis step are shown in [Scheme 1](#). The different pathways for the ring opening mechanism in the presence of ammonia are depicted in [Scheme S1](#) (see Supplementary Information). [Scheme S2](#) revises the effective synthesis mechanisms leading to different ratios of insertion (mono- vs. di-substitution).

2.3. Materials characterization

Elemental analysis was analyzed using a Micro Corder JM10



Scheme 1. The synthesis of acetate- and phosphonate- polyglycidyl methacrylate (PGMA).

automated analyzer (J-Science Lab Co., Ltd., Kyoto, Japan). FTIR spectra were obtained in the 4000–400 cm^{-1} range, using a Nicolet iS10 FTIR-spectrometer (Thermo Fisher Scientific, Waltham, MA, USA). The X-ray diffraction (XRD) was examined using a SmartLab X-Ray Diffractometer (RIGAKU, Japan). A thermogravimetric and differential thermal analyzer EXSTAR 6000 TG/DTA 6300 N was used for TG/DTA (Seiko Instruments Inc., SII, Chiba-Shi-Chiba, Japan). The pH-drift technique was used to measure the sorbent particles' point of zero charge (pH_{PZC}): the sorbents were agitated for 24 h to equilibrate with a series of NaCl solutions (0.1 M) with varying the initial pHs (pH_i); the equilibrium pH (pH_{eq}) was recorded and the pH_{PZC} is in line with $\Delta\text{pH} = 0$ [39].

2.4. Sorption studies

Batch tests were completed and performed in a glass bottle by contacting a given mass (m, g) of sorbent with a constant volume (V, L) with a definite concentration (C_0 , 50 mg Nd L^{-1}) at an initial pH value (pH_0). The sorbent dose, $\text{SD} = m/V$, is fixed at 0.5 g L^{-1} . The mixtures were agitated at 200 rpm for 3 h at room temperature ($T: 26 \pm 1$ °C). After equilibration and phase separation, the initial and equilibrium Nd(III) concentrations: C_0 and C_{eq} , (mg Nd L^{-1}) were determined by ICP-OES (Inductively Coupled Plasma Optical Emission Spectrometer, Prism ICP, Teledyne Leeman Labs., Hudson, NH, USA). The equilibrium sorption capacity (q_{eq} , mg Nd g^{-1}) was determined using the equation: $q_{\text{eq}} = (C_0 - C_{\text{eq}}) V/m$. The distribution ratio (D, L g^{-1}) corresponds to $D = q_{\text{eq}}/C_{\text{eq}}$. The pH was adjusted before sorption to the desired value (i.e. initial pH), and after the equilibrium attained, the equilibrium pH (pH_{eq}) was systematically recorded. The agitation speed was set to 200 rpm.

For the study of pH effect, the initial pH (pH_0) varied from 1.0 to 6.0: a specific volume of solution was combined with a constant mass of sorbent ($\text{SD}: 0.5 \text{ g L}^{-1}$). Isotherms studies were investigated at different initial concentrations (0.17–2.77 mmol Nd L^{-1} , at $\text{pH}_0: 4.5$) at four temperatures (i.e. $298 \pm 1 \text{ K}$, $308 \pm 1 \text{ K}$, $318 \pm 1 \text{ K}$ and $328 \pm 1 \text{ K}$); the duration of contact was set for 4 h. To assess uptake kinetics, the samples were analyzed at constant times at different time intervals (in the range: 5–360 min); at initial concentration ($C_0: 0.693 \text{ mmol Nd L}^{-1}$) and the SD was 0.5 g L^{-1} .

A preliminary investigation tested different eluents types in batch systems using 0.5 M acid solutions (HCl, H_2SO_4 and HNO_3), under agitation for 90 min at 26 °C ($\text{SD}: 1 \text{ g L}^{-1}$). To test sorbent recycling, Nd-loaded sorbents were mixed with HNO_3 (0.5 M) (under constant agitation at room temperature). Five sorption and desorption successive cycles were performed (including a rinsing step between each operation) and compared to the first cycle's value. The equation that describes desorption efficiency ($\text{DE} = C_{\text{D}} \times V_{\text{L}} \times 100 / q_{\text{d}} \times m_{\text{d}}$) and regeneration efficiency ($\text{RE} = q_{\text{d}} \times 100 / q_{\text{e}}$) were systematically calculated. C_{D} (mg Nd L^{-1}) is.

Nd(III) concentration in the eluate, $V(\text{L})$ is the eluent volume, q_{d} (mg Nd g^{-1}) is the sorption capacity at each stage before desorption experiment, q_{e} (mg Nd g^{-1}) is the initial sorption capacity (at first cycle) and m_{d} (g) is the sorbent mass utilized in desorption experiments.

Table S1 summarizes the models used for fitting uptake kinetics and sorption isotherms. Non-linear regression analysis was used for the determination of relevant model parameters.

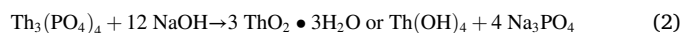
Annex A shows the repeatability of sorption tests for A-PGMA and P-PGMA sorbents.

2.5. Application to pre-treated leachate of Egyptian monazite ore

The application of sorbents was performed on alkaline leachates of monazite ore samples collected from Abou-Kashaba coast (black beach sands), near Rosetta (Rashid City, close to Alexandria, Beheira Governorate, Egypt). Monazite is an orthophosphate mineral associated with rare earth elements and thorium. Rare earth oxides represent about 60% of the mineral and are mostly formed of LREEs (light REEs). The analysis of Egyptian monazite (97%) showed the following composition: ThO_2

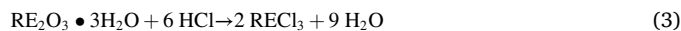
(5.9%), U_3O_8 (0.44%), Ce_2O_3 (26.55%), while other rare earth oxides (REE_2O_3) account for 34.35%. The mineral is characterized by a specific gravity close to 4.9–5.3 g cm^{-3} , while its harness ranges between 5 and 5.5 (Moh's scale) [40–42].

Although monazite may be commercially treated by either acid or alkaline leaching for metal extraction; alkaline leachates are frequently preferred, mainly for economic competitiveness and easiness of management. Indeed, the requested temperature is usually lower than for acidic leaching. In addition, the sub-products (trisodium phosphate) can readily be valorized as fertilizer [43]. The alkaline leaching can be schematized according [41] to Eq. 1–2:



The hydrous/oxide concentrate (obtained from alkaline thermal processing of monazite) is leached with HCl acid solution at 80 °C, before being diluted with water. Thorium (and uranium) may be separated from REEs by selective neutralization steps with ammonia solution or alkali (pH controlled to 5.8–6, [40–42]). Rare earth concentrate is recovered by selective neutralization, rising the pH to 8.0–8.2.

For the study of sorption properties, RE chloride solution was obtained from HCl digestion of the rare earth oxide concentrate (1 g) with 1 M HCl solution (10 mL), at 80 °C, for one hour; the volume of the solution was finally adjusted to 200 mL. The reactions may be schematized according to Eq. 3–4:



The sorption tests were performed in batch reactor ($v: 200 \text{ rpm}$) with the main objective of evaluating the effect of the complexity of the solution on the recovery of neodymium among the REEs series. The experimental conditions were not selected for recovering the totality of REEs. The pH of the pre-treated leachate was set to 4.02 using sodium carbonate/bicarbonate for pH control [44]. The sorbent dose was set to 0.5 g L^{-1} ; the temperature was fixed to 55 ± 1 °C. After equilibrium (i.e., 2 h), the solution was filtrated and analyzed for determination of the residual concentrations of REEs, using ICP-AES.

2.6. Molecular modeling – DFT calculations

Density functional theory (DFT) calculations were carried out by the metahybrid GGA functional M06-2x [45], as recommend for lanthanides [46], combined with the def-TZVP basis set by Ahlrics et al. [47,48]. For description of the core electrons of Nd, a relativistic effective core potential of 28 electrons was used [49]. Due to the quadruplet ground state of Nd, unrestricted formalism was employed. Bond orders were calculated by Mayer bond order analysis using Multiwfn program [50]. Gaussian 16 software was used for all other calculations [51]. Calculations were carried out in water medium by the SMD variation of the polarizable continuum model (PCM) [52]. We also attempted gas-phase calculations with explicit inclusion of water molecules in 8- and 9-coordinate coordination spheres [53], but the PCM calculations turned out more robust. Harmonic vibrational frequency analyses proved optimized structures as potential energy surface actual minima; Gibbs free energies were determine at $T = 298 \text{ K}$ and $p = 1 \text{ atm}$.

3. Results and discussion

3.1. Materials characterization

3.1.1. Pathways for the synthesis of A-PGMA and P-PGMA

The synthesis procedures for A-PGMA and P-PGMA sorbents are shown in Scheme 1. PGMA (micro-particles < 75 nm) was prepared using the dispersion polymerization process.

By opening the epoxide ring and reacting with ammonia ($\text{NH}_4\text{O}-\text{H}_{(\text{aq.})}$) solution, PGMA is functionalized with $-\text{NH}_2$ groups ($\text{NH}_4\text{OH}_{(\text{aq.})} \rightarrow \text{NH}_3 + \text{H}_2\text{O}$ at 60°C) for the N-PGMA synthesis (Scheme S1).

Scheme S1 depicts two routes (A (SN^1) and B (SN^2)) that might be implicated in the three-membered epoxy ring nucleophilic attack on N-atom in terminal $-\text{NH}_2$. According to pathway A, the epoxy ring opening is regioselective (at the interior C-atom), resulting in internal secondary carbonium ion that is more stable. While, in pathway B, the N-atom attack, which happens preferentially onto the exterior carbon (less sterically obstructed); the main less stable carbonium ion is formed. The aminated (N-PGMA) synthesis is more favorable and easier via pathway A [54,55].

In a second step, the carboxymethylation reaction (A-PGMA) proceeds through a condensation of monochloroacetic acid with amine group under basic conditions: as a by-product, HCl is produced, lowering the pH of the solution from 9.7 to 4.9 when the procedure is completed [38]. For the synthesis of P-PGMA, when formaldehyde is present, phosphonic acid is reacted with amine functionalities (N-PGMA); methylene phosphonic groups are grafted [38].

N-carboxymethylation and N-phosphonomethylation of N-PGMA have been revised (Scheme S2). According to the N-methylcarboxylation and phosphonomethylation mechanism: for polysubstituted structure, one or two carboxymethyl/phosphonomethyl moieties can be grafted on the main amine group ($-\text{NH}_2$): both mono- and di-substituted amine are acceptable. However, elemental analysis data showed that P (wt%) is lower than expected compared with the C, H, N elements content. This means that the mono-phosphomethylated product was preferentially formed, most likely due to steric hindrance effect controlled by pending groups.

3.1.2. Morphology of PGMA particles and its textural features

SEM image of PGMA particles is shown in Fig. S1. This figure shows massive objects with irregular size. The image software (Foxit PhantomPDF) allowed evaluating the distribution of particle sizes (appearing in the same figure). The particles are roughly and irregularly spherical. The average particle size is evaluated to $58.3 \pm 8 \mu\text{m}$. Fig. S2 shows the XRD patterns of pristine and functionalized PGMA materials. The XRD profiles are poorly resolved, consistently with the weak crystallinity of PGMA substrate. A main peak is observed at $2\theta = 17.7^\circ$; while weak and broad shoulder can be identified at $2\theta = 9.5\text{--}13^\circ$, $28\text{--}31^\circ$ and $40\text{--}44^\circ$; these peaks are consistent with the XRD fingerprint of amorphous PGMA [19]. The substitution of PGMA via aminocarboxymethylation and aminophosphonomethylation potentially increases the disorder in the polymer structure: the relative reduction in the intensity and width of XRD peaks confirms this, though the general structure is maintained (with detection of peaks at angles close to the values reported for pristine PGMA).

The textural characteristics have been determined by N_2 adsorption/desorption isotherms for two functionalized sorbents (A-PGMA and P-PGMA), which were prepared from the same parent polymers PGMA (precursor) (i.e. with the same textural characteristics including pore structure and surface area) (Fig. S3). Hence, any subsequently changes in the textural properties mainly related to the functionalization step and its impact on the structure. The two derivatives of PGMA show very similar profiles, which can be qualified as Type II isotherms according Langmuir classification. Both A-PGMA and P-PGMA show a hysteresis loop. According elemental analysis (see below, the higher degree of substitution (methylcarboxylate groups) for A-PGMA (compared with phosphonomethylation of P-PGMA) increases the steric hindrance, which, in turn, may explain the slightly lower specific surface area (95.4 vs. $114.5 \text{ m}^2 \text{ g}^{-1}$) and smaller pore size (78 \AA vs. 84 \AA). It is noteworthy that these orders of magnitude are consistent with the values reported for polyaminated PGMA materials (i.e., $125.5\text{--}136.5 \text{ m}^2 \text{ g}^{-1}$) [56].

3.1.3. Thermogravimetric depiction

Fig. S4 depicts the thermogravimetric characteristics of PGMA

derivatives (compared with pristine PGMA). Substantial differences can be identified in terms of weight loss and number of degradation steps (Fig. S4a) but also in the DTG diagrams (Fig. S4b). While PGMA is characterized by a negligible loss of water ($<2\%$) in the initial step (below 120°C), the other derivatives show a water loss ranging between 8% (A-PGMA) and 13% (P-PGMA): the derivatives are obviously more hydrophilic than pristine support. The DTG curves show clearly identified valleys at: $\sim 46.5^\circ\text{C}$ and $\sim 50.4^\circ\text{C}$, respectively. The degradation profile of PGMA is similar to that described by Caykara et al. [57] and Yu et al. [58]: a strong weight loss is observed between 230°C and 430°C corresponding to the degradation of the polymer; the residual mass is below 4% , while the total degradation is reported at 900°C . The DTG curve shows three valleys at $\sim 247.9^\circ\text{C}$, $\sim 344.6^\circ\text{C}$ and $395\text{--}403^\circ\text{C}$, associated with the changes in the slope of the TGA curve and with the depolymerization of PGMA, the degradation of ester links, the degradation of shortened chains with formation of chars and finally the thermal degradation of the char (last degradation section). The DTG peaks are more marked than those reported by Caykara et al. [57], who only identified the random chain scission peak at $\sim 301^\circ\text{C}$.

For functionalized PGMA, apart the difference in water release at low temperature, different transitions can be observed. In the case of A-PGMA, two main steps are observed:

(a) between 235°C and 450°C (weight loss, WL: about 40% ; total weight loss, TWL: $\sim 56\%$), associated with the decomposition of amine arm grafted on PGMA, degradation of acetate groups,

(b) between 450°C and 825°C (WL: $\sim 17\%$; TWL: $\sim 73\%$), corresponding to the pyrolysis of the char. The residue represents around 27.2% .

These transitions are associated with 2 DTG valleys at $\sim 282.5^\circ\text{C}$ and $\sim 693.3^\circ\text{C}$, respectively. A weak shoulder is also observed close to $370\text{--}430^\circ\text{C}$.

In the case of P-PGMA, three main steps are identified associated with depolymerization and degradation of ending groups (i.e., phosphonate):

(a) between 235°C and 335°C (WL: $\sim 28\%$; TWL: $\sim 44\%$),

(b) between 335°C and 460°C (WL: $\sim 34\%$; TWL: $\sim 78\%$),

(c) above 460°C , the thermal degradation of the char represents an additional weight loss of 8% .

It's worth noting that grafting reactive groups enhances the material's thermal stability significantly, particularly when iminoacetate groups are formed. At 900°C , the residues represent about 0.5% , 14% , and up to 27.3% for PGMA, P-PGMA, and A-PGMA, respectively. These differences between A-PGMA and P-PGMA may reflect the higher thermal stability of the iminoacetate derivative and/or the higher density of the substitution with acetate-based sorbent, which could, in turn, affect the reactivity and/or accessibility (controlled by steric hindrance) of the reactive groups on the sorbents.

3.1.4. FTIR characterization of sorbents

The FTIR spectra of pristine PGMA and successive compounds (intermediary N-PGMA, A-PGMA and P-PGMA) are reported in Fig. 1. Substantial changes are identified in the $3600\text{--}3000 \text{ cm}^{-1}$ range; this spectrum window usually corresponds to contributions from $-\text{OH}$ (and H_2O traces) and $-\text{NH}$ groups. As expected based on the chemical structure of PGMA (no $-\text{NH}$ and $-\text{OH}$ groups and its hydrophobic behavior), the spectrum is poorly resolved in this window (hydrophobic polymer) and shows a weak band at 3505 cm^{-1} . The bands at 2933 cm^{-1} and 2998 cm^{-1} can be assigned to CH stretching (in methyl groups, symmetric and asymmetric, respectively). The weak band at 3061 cm^{-1} is attributed to the residual contribution of olefinic $\text{C}=\text{C}$ bond; its weak intensity clearly demonstrates the efficient polymerization of GMA. The strong band at 1721 cm^{-1} is representative of $\text{C}=\text{O}$ stretching vibration [59]. Other signals systematically found in PGMA-based polymers are identified at: 1482 cm^{-1} and 1447 cm^{-1} (deformation of OH and symmetric stretching of COO^-), 1340 cm^{-1} (primary $-\text{OH}$ stretching), 1253 cm^{-1} ($\text{C}-\text{C}$ stretching), 1163 cm^{-1} ($\text{C}-\text{O}$ stretching), 1146 cm^{-1} and

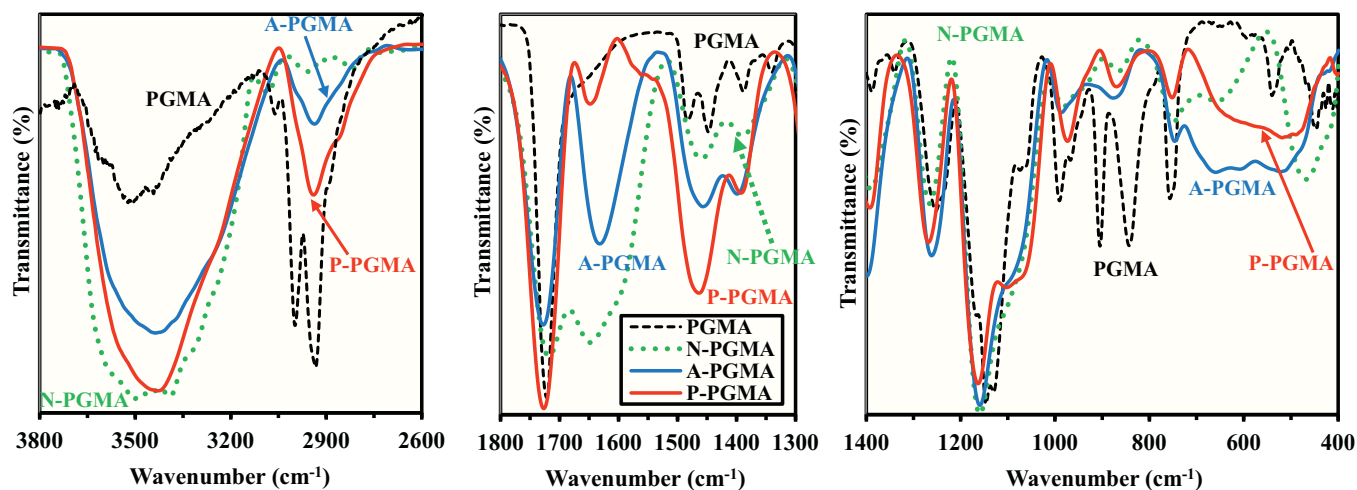


Fig. 1. FTIR spectra of PGMA, A-PGMA, and P-PGMA (N-PGMA is also reported as intermediary support).

1130 cm^{-1} (stretching C-OH in primary alcohol and C—O stretching from ester group), 1074–1061 cm^{-1} (secondary —OH stretching), 905 cm^{-1} and 843 cm^{-1} (stretching of C-O-C in epoxy), 757 cm^{-1} (epoxide ring) [35,37,60]. The bands at 1388 cm^{-1} (due to, primary alcohol —OH bending), 990 cm^{-1} (P-OH), 967 cm^{-1} (P-OH) can be associated with the phosphonate moieties [61]. The medium/wide band at 540 cm^{-1} is attributed to the out-of-plane bending mode (C-C-N) (in the reference paper it was identified at 568 and 536 cm^{-1} [62]).

The functionalization of PGMA induces many changes, including the appearance of a broad band in the 3600–3000 cm^{-1} range: the amination of PGMA is followed by the appearance of —OH and —NH groups leading to a broad band, with a series of weak extrema (at 3505 cm^{-1} and 3392 cm^{-1} , associated with —NH stretching). On the other side, for A-PGMA, the broad band (with a maximum at 3436 cm^{-1}) corresponds to the increase in the density of —OH groups (consistently with Scheme S2); at ~3250 cm^{-1} : a shoulder was detected. In addition, the chemical modification brings to the polymer a hydrophilic behavior and the appearance of —OH stretching vibration (from water adsorption). In the case of P-PGMA, similar pattern can be observed with the reinforcement of the contribution associated with —OH groups (at ~3429 cm^{-1}), while the shoulder at ~3061 cm^{-1} decreases. The C—H stretching in methyl groups is maintained at 2938 cm^{-1} for A-PGMA and P-PGMA (strongly reduced for N-PGMA); however, the others signals (especially the band at 2998 cm^{-1}) associated with methyl CH stretching vibrations are significantly reduced (almost disappearing for N-PGMA). The vibration of residual olefinic groups is shifted to 3084 cm^{-1} .

The C=O stretching vibration is maintained around $1714 \pm 2 \text{ cm}^{-1}$. The vibration at 1253 cm^{-1} (C—C stretching) is shifted to higher wavenumbers (in the range 1268–1261 cm^{-1}) after chemical grafting onto PGMA. Similar shift is observed for the band at 1388 cm^{-1} (which can be attributed to CH_3 sym. Def. and or —C-O str., in primary alcoholic group, [63]). The band at 1144 cm^{-1} (C—O stretching) is red-shifted to 1160 cm^{-1} after carboxylation and phosphonation. The band at 1447 cm^{-1} (COO— stretching) is shifted to 2464–1457 cm^{-1} .

The bands in the range 1200–1020 cm^{-1} are roughly maintained after chemical modification. The band at 757 cm^{-1} is blue-shifted (to 746 cm^{-1}). The most notable variations are at 1339, 990, 540, and 445 cm^{-1} , that decrease in intensity and even disappear. The bands at 905 cm^{-1} and 843 cm^{-1} , which were very strong in the case of PGMA, completely disappear after grafting: these peaks are assigned to the epoxy group (C-O-C stretching); this disappearance means that the grafting was very efficient and quantitative [35,38]. Epoxide groups are cleaved and transformed to hydroxyl and amine groups [64].

The main modifications associated with amination of PGMA are characterized by the specific appearance of a weak band at 1648 cm^{-1}

(corresponding to N—H bending vibration in secondary amine and/or primary amine band — *in plane* deformation): this band is shifted to 1631 cm^{-1} in A-PGMA (being masked by a broad band) and is strongly reduced after phosphonation (in P-PGMA). This might be also explained by the significant contribution of carboxylate groups in A-PGMA (broad and intense band) [64]. The phosphorylation is demonstrated by the emergence of weak bands at 752 cm^{-1} (P-O-C or P—C stretching), 974 cm^{-1} (P-O-C or P-OH stretching), 1268 cm^{-1} (P=O bond) [36,61]. On the other hand, the carboxylation of N-PGMA involves the reinforcement of the band at 1399 cm^{-1} as well as the appearance of a broad and intense band at 1632 cm^{-1} ; these signals are associated with carboxylate moieties. FTIR spectra clearly demonstrate the efficient functionalization (amination) of PGMA support and the successful carboxymethylation and phosphonomethylation of aminated PGMA.

3.1.5. Elemental analysis and pH_{PZC} determination

The elemental analyses of PGM and the successive derivatives are summarized in Table S1. The successful amination is confirmed by the appearance of nitrogen (2.56 mmol N g^{-1}). However, based on the O and N contents (i.e., 24.37 mmol O g^{-1} and 2.56 mmol N g^{-1}) and the structure of PGMA (3 O per unit), the grafting yield can be evaluated to 31.5% (2.56 N per 8.12 PGMA units). The same calculation based on C content (i.e., 41.36 mmol C g^{-1} and 2.56 mmol N g^{-1}) gives a much higher grafting yield, close to 61.9% (i.e., 2.56 N per 4.14 PGMA units). The actual fractions of C, H and N elements decrease with the carboxymethylation of N-PGMA, contrary to O element. According the suggested structure for A-PGMA (i.e. 4 additional O per amine group, or N), the complete functionalization would bring an additional O content close to 6.4 mmol g^{-1} ; actually, the increase in O content is 5.16 mmol O g^{-1} . This reveals that the grafting yield may be ~ 80.6% (calculated from N content in A-PGMA). The phosphonomethylation of PGMA also decreases the C, H and N elements relative fractions, while O content increases, due to the insertion of 3 O (2 —OH and 1 = O) per amino unit. The P content only reaches 0.56 mmol P g^{-1} (vs. 1.41 mmol N g^{-1}); this means that the rate of substitution does not exceed 39.7%. The increase in O content (compared with N-PGMA) is close to 5.94 mmol g^{-1} ; this is far above (i.e., a factor 10.6) from expected variation (based on the stoichiometry 3 O per P, in the suggested structure of the derivative).

These data should be considered indicative; indeed, PGMA is hydrophobic, the functionalization brings a hydrophilic behavior to the polymer. It is noteworthy that the elemental analysis of second batches of sorbents shows that the synthesis is reproducible.

Table S2 also reports the pH_{PZC} values of the materials (deduced from pH-drift method, Fig. S5). As expected, the grafting of basic groups (amination) increases the pH_{PZC} of PGMA, which is shifted toward

higher values (i.e., 5.84 to 7.53). The pK_a of ammonia and primary amines is close to 9 [65]. In contrast, the pH_{PZC} values are decreased while grafting acid moieties: 4.51 for P-PGMA and down to 3.38 for A-PGMA. The carboxylic acid groups have pH_{PZC} values lower than those of phosphonate-based groups: Carboxylic and phosphonic acid groups' acidity is closely related to the difference in pH_{PZC} values. This is apparently opposite to data previously reported: with pK_{a1} 0.5–1.5 and pK_{a2} 5–6, α -aminophosphonic is a more powerful diacid, compared to mono-carboxylic acid acidity (~ 2.2 –3) [65,66]. Furthermore, the phosphonic acid groups versus carboxylic acid groups substitution degree accounts for this disparity. The atomic radius of phosphorus is much bigger than that of carbon [38,65–67], the steric action of phosphorus prevents N-bearing di-substituted phosphorylated material from forming. So, the phosphomethylation reaction is mono-substitution mode, whereas the carboxymethylation reaction is di-substitution one.

3.2. Sorption and desorption studies

3.2.1. Effect of pH

The pH is a critical parameter for the sorption of metal ions. Indeed, the pH influences both the chemistry of metal ions in the solution (hydrolysis, formation of polynuclear species, etc.) and the surface charge of the sorbent. This balance of effects directly influences sorption efficiency and sorption capacity. In some cases, playing with the pH may also influence the mechanisms of metal sorption (i.e., chelation vs. ion exchange/electrostatic attraction). The progression of sorption capacity vs. equilibrium pH is shown in Fig. 2. At a pH ~ 0.85 , the sorption capacity of both sorbents is extremely low (within the range 0.05–0.08 mmol Nd g^{-1}). At this pH, the sorbents are systematically protonated; which induces the repulsion of cationic Nd(III) species. Indeed, the metal speciation calculation under particular experimental settings (using Visual Minteq, [68]) demonstrates that Nd(III) is present as free Nd^{3+} on the whole pH range of this study: hydrolyzed species appear at pH 5; however, even at pH 6, $NdOH^{2+}$ represents $<0.6\%$ of total neodymium. In any case, the metal is present as cationic species, which may be repulsed by strongly protonated reactive groups. Increasing the pH significantly improves the sorption of Nd(III): almost linearly for P-PGMA and with a strong inflexion above pH 2 for A-PGMA. As pH rises, the protonation of reactive groups reduces: the repulsion of Nd^{3+} diminishes and the sorption increases up to 0.36 mmol Nd g^{-1} at $pH_{eq} \sim 4.0$ for A-PGMA and 0.42 mmol Nd g^{-1} at $pH_{eq} 4.42$ for P-PGMA. Actually, P-PGMA is slightly better than A-PGMA in the medium range of acidic pH values (i.e., pH_{eq} 2–3.5); the differences are less marked in mild acidic conditions. In the case of A-PGMA, the sorption increases more significantly above its pH_{PZC} (i.e., 3.38). For N-PGMA (as

reference) the sorption is still quite low (i.e., below 0.07 mmol Nd g^{-1}) on a broad pH range (i.e.; from pH_{eq} 0.94 to 4.42).

Fig. S6a shows the distribution ratio (defined as $D = q_{eq}/C_{eq}$), in \log_{10} unit, vs. equilibrium pH. The P-PGMA curve is linearly fitted with a slope close to 0.319 (determination coefficient, R^2 : 0.996). This slope is related to the stoichiometry of proton exchange in ion-exchange reactions; herein, this fits with the exchange of 3 protons per bound Nd^{3+} (theoretical slope: 0.333). For the two other systems, the linear fits partially fails (especially for N-PGMA) because of very low sorption capacities at low pH values: R^2 values are much lower (i.e., 0.975 or 0.946) and the slopes are close to 0.297 and 0.173. While taking into account only the pH values where sorption capacity is significantly increased (corresponding to pH-range of linearity of $\log_{10} D$ vs. pH_{eq}), the linear fits approach the expected trends with slopes close to 0.346 (R^2 : 0.991) and 0.288 (R^2 : 0.986). Under favorable pH conditions, Nd(III) sorption is accompanied by the stoichiometric release of 3 protons (from protonated reactive groups). The change in pH variation during the sorption process is depicted in Fig. S6b. This is crucial information since the three sorbents have shown substantial differences in the pH-drift titration experiment, associated with large variations of the pH_{PZC} . In the case of P-PGMA and A-PGMA, the equilibrium pH remains relatively stable (variation by <0.5 pH unit) on a wide range of pH (i.e., 1.1 to 4); above, the equilibrium pH decreases by up to 1.8–1.4 pH unit at pH_0 6 (with a progressive plateau in pH variation). The pH variation is globally more marked for P-PGMA than for A-PGMA, consistently with the values of pH_{PZC} (i.e., 3.38 and 4.51, respectively). A completely different trend is observed for N-PGMA, where pH variation was much more important: the pH (pH 1–2) remains stable and drastically increases above pH 2, where the pH increases by about 1.5 pH unit. The basic behavior of grafted amine groups imposes a global basic behavior to the sorbent (i.e., neutralization by proton binding and strong pH variations). The increase of the pH may involve precipitation phenomena at high pH value and high metal concentration. This could explain the second wave in sorption capacity observed at $pH_{eq} > 6$ in Fig. 2.

The comparison of the curves shows that in terms of affinity for Nd(III), the sorbents might be ordered as follows: P-PGMA $>$ A-PGMA $>$ N-PGMA. Further studies will confirm these trends (see Section 3.2.3.).

3.2.2. Uptake kinetics

The uptake kinetics can be influenced by several mechanisms, including the appropriate sorption rate (frequently associated with first- and second-order rate equations, by analogy with homogeneous chemical reactions) and according to mass transfer criteria (includes bulk, film and intraparticle diffusion resistances). The rate coefficient should be regarded an apparent rate constant for extrapolating the first- and second-order rate equations to heterogeneous systems (implicitly include the role of mass transfer resistance effects); meaning PFORE (pseudo-first order rate equation) and PSORE (pseudo-second order rate equation). The specific mass transfer mechanisms can be influenced by the sorbent particles size, textural properties and the sorbent affinity toward metal ions of interest, as well as external physical conditions like agitation speed and temperature. According to preliminary testing, a velocity of around 200 rpm avoids bulk diffusion resistance and reduces the influence of film diffusion limitations.

In this study, the fraction 50–75 μm was used to reduce intraparticle diffusion resistance. However, the kinetic profiles show that 180 to 240 min of contact are required to attain equilibrium (Fig. 3). Apparently, despite the sorbents micrometric size, it appears that resistance to intraparticle diffusion resistance is a factor that must be considered (faster equilibrium would be expected for such small particles). As expected, P-PGMA allows higher removal of Nd(III); the sorption capacities at equilibrium reach 0.560 and 0.628 mmol Nd g^{-1} for A-PGMA and P-PGMA, respectively. These values represent about 86% of the sorbents maximal sorption capacity (see Section 3.2.3.1); this means that, under these experimental conditions, the sorbents are almost saturated. This also means that the interpretation of kinetic fits may be considered

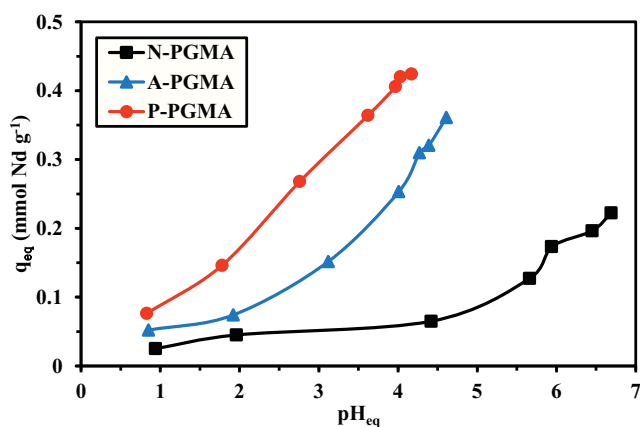


Fig. 2. Effect of pH_{eq} on the sorption of Nd(III) using N-PGMA, A-PGMA, and P-PGMA (C_0 : 0.347 mmol Nd L^{-1} ; SD: 0.5 $g L^{-1}$; Time: 720 min; T: 26 $^{\circ}C$; v: 200 rpm).

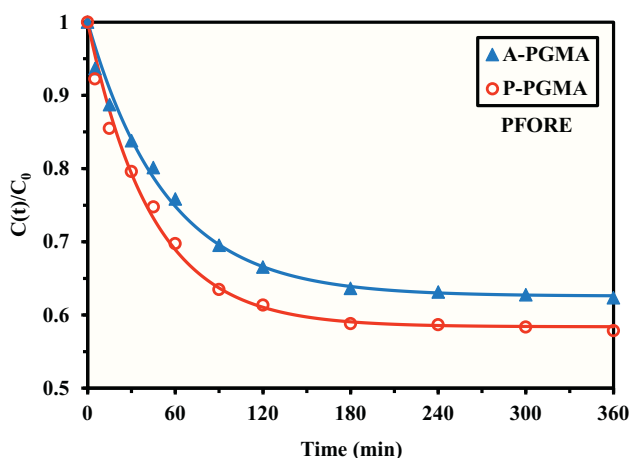


Fig. 3. Uptake kinetics of Nd(III) using A-PGMA and P-PGMA – Using the PFORE for modeling (pH_0 : 4.63; SD: 0.5 g L^{-1} ; C_0 : $0.744 \text{ mmol Nd L}^{-1}$; T: $26 \text{ }^\circ\text{C}$; v: 200 rpm).

carefully. Hubbe et al. [69] critically commented the interpretation of kinetic modeling in relation with inappropriate selection of experimental conditions (and notably the importance of maintaining relatively constant the concentration in the batch for applying, for example, the pseudo-second order rate equation). Simonin [70] also reported the difficulty in assigning mathematical fits to mechanistic interpretations when the experimental design is not appropriate. Table 1 reports the PFORE and PSORE parameters [71] and RIDE (obtained from the Crank equation for intraparticle diffusion resistance, [72]). The selection of the best fits is based on several criteria such as the determination coefficient (R^2), the Akaike information criterion (AIC, which considers the amount of parameters that may be changed), and also the coherence between the experimental sorption capacity value at equilibrium ($q_{\text{eq,exp}}$, mmol g^{-1}) and the fitted value (i.e., $q_{\text{eq,1}}$ or $q_{\text{eq,2}}$, mmol g^{-1}). In Fig. 3, the solid lines are the PFORE experimental data fits (while Fig. S7 shows the fits with the PSORE and the RIDE). Apparently, the statistical parameters are very close for the different models: the $|\Delta\text{AIC}|$ must be >2 for demonstrating a significant difference. Therefore, the PSORE can be considered a little less precise, when modeling of experimental profiles.

This is also demonstrated by the significant disparity between experimental and fitted values of the sorption capacities at equilibrium: $|\Delta q_{\text{eq}}|$ is in the range 12.7–16.6% for PSORE while it does not exceed 1.4% for PFORE. The AIC values are a little lower for RIDE than for PFORE. These trends show that the PFORE can finely fits kinetic profiles and that the resistance to intraparticle diffusion is important to keep the sorption process under control. This is also confirmed by the value of the effective diffusivity coefficient in the sorbents, which ranges between

Table 1
Modeling of uptake kinetics for Nd(III) sorption using A-PGMA and P-PGMA sorbents.

Model	Parameter	Sorbent	
		A-PGMA	P-PGMA
Experimental	$q_{\text{eq,exp}}$ (mmol Nd g^{-1})	0.560	0.628
PFORE	$q_{\text{eq,1}}$ (mmol Nd g^{-1})	0.557	0.619
	$k_1 \times 10^2$ (min^{-1})	1.86	2.29
	R^2	0.994	0.994
	AIC	-101	-99
PSORE	$q_{\text{eq,2}}$ (mmol Nd g^{-1})	0.653	0.708
	$k_2 \times 10^2$ ($\text{g mmol}^{-1} \text{ min}^{-1}$)	3.35	4.11
	R^2	0.991	0.991
	AIC	-100	-99
RIDE	$D_e \times 10^{12}$ ($\text{m}^2 \text{ min}^{-1}$)	5.39	6.24
	R^2	0.992	0.994
	AIC	-103	-105

$5.4 \times 10^{-12} \text{ m}^2 \text{ min}^{-1}$ and $6.2 \times 10^{-12} \text{ m}^2 \text{ min}^{-1}$; this is a four-order-of-magnitude reduction in comparison to the free diffusivity of Nd(III) in water (i.e., $3.7 \times 10^{-12} \text{ m}^2 \text{ min}^{-1}$, [73]). The diffusivity in P-PGMA is a little faster than in A-PGMA. This is also documented by the comparison of the apparent rate coefficient (i.e., k_1) that slightly increases from $1.86 \times 10^{-2} \text{ min}^{-1}$ to $2.29 \times 10^{-2} \text{ min}^{-1}$.

3.2.3. Sorption isotherms and thermodynamics

3.2.3.1. Effect of reactive groups on sorption isotherms. Sorption isotherms reflect, at a constant temperature and pH value, the equilibrium solute distribution between liquid and solid phases (i.e., $q_{\text{eq}} = f(C_{\text{eq}})$). Fig. 4 compares Nd(III) sorption isotherms at pH_0 4.5 for N-PGMA, A-PGMA and P-PGMA. The benefit of functionalization of N-PGMA clearly appears; the maximum sorption capacity is more than doubled after carboxymethylation and phosphonomethylation. The affinity range confirms the trends observed while investigating the effect of pH:

Maximum sorption capacity (mmol Nd g^{-1}): N-PGMA (0.304) $<$ A-PGMA (0.645) $<$ P-PGMA (0.736).

In addition, the initial slope, which may be related to the sorbent affinity for metal ion, is also substantially enhanced (especially for P-PGMA).

The Langmuir, Freundlich, Sips and Temkin equations were used to simulate the sorption isotherms (see Table S1). Table 2 reports the statistical analysis of mathematical fittings. The asymptotical shape of the isotherms means that the sorbent progressively saturates, which is contradictory with the exponential trend of the Freundlich equation (considering that the sorption energies are heterogeneous, that sorbed molecules may interact and that sorption may occurs through multi-layer). The three other equations give good fits for experimental data, especially the Langmuir equation (solid curves in Fig. 4) and the Sips equation (solid curves in Fig. S8).

The Sips equation is a mathematical equation combining the Langmuir and the Freundlich equations. Usually adding a supplementary adjustable parameter improves the quality of the fit. However, using the AIC allows showing that the benefit of this third adjustable parameter is not statistically significant.

The maximum sorption capacity (at monolayer saturation; i.e., $q_{\text{m,L}}$, mmol Nd g^{-1}) also follows the ranking:

N-PGMA (0.338) $<$ A-PGMA (0.732) $<$ P-PGMA (0.776).

The sorbents can be also ranked in the same order, considering the coefficient of affinity (b_{L} , L mmol^{-1}):

N-PGMA (3.94) $<$ A-PGMA (5.43) $<$ P-PGMA (9.59).

Neodymium is classified as a hard acid; according the HSAB (hard and soft acid and bases principle, [74]), hard acids prefer to associate with hard bases. On the other hand, both primary and secondary amine groups (N-ligand atom) are considered as intermediary bases, while both carboxylate and phosphonate moieties (O-ligand atom) are ranked

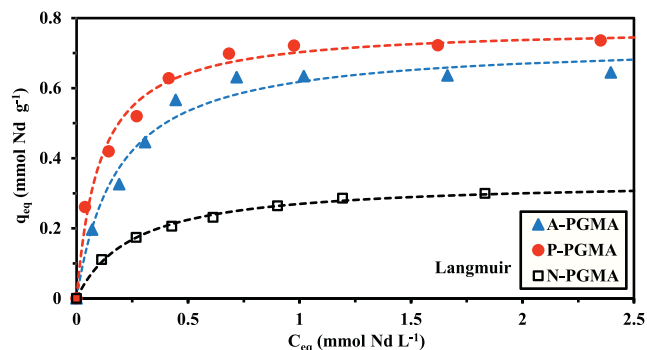


Fig. 4. Comparison of Nd(III) sorption isotherms using N-PGMA, A-PGMA, and P-PGMA – Using the Langmuir equation to model (C_0 : $0.17\text{--}0.72 \text{ mmol Nd L}^{-1}$; SD: 0.5 g L^{-1} ; pH_0 : 4.5; T: $26 \pm 1 \text{ }^\circ\text{C}$; time: 4 h; v: 200 rpm).

Table 2

Modeling of Nd(III) sorption isotherms using A-PGMA and P-PGMA sorbents at different temperatures.

Model	Temperature		T: 26 °C			T: 35 °C		T: 45 °C		T: 55 °C	
	Parameter	Sorbent	N-PGMA	A-PGMA	P-PGMA	A-PGMA	P-PGMA	A-PGMA	P-PGMA	A-PGMA	P-PGMA
Experimental	$q_{m,exp}$		0.304	0.645	0.736	0.676	0.756	0.714	0.799	0.738	0.839
	$q_{m,L}$		0.338	0.732	0.776	0.762	0.800	0.791	0.837	0.813	0.873
Langmuir	b_L		3.94	5.43	9.59	6.14	10.3	7.01	11.4	7.45	13.6
	R^2		0.985	0.979	0.988	0.982	0.987	0.986	0.965	0.986	0.961
	AIC		-65	-56	-59	-56	-58	-45	-57	-43	
	$q_{m,S}$		0.352	0.686	0.824	0.726	0.844	0.760	0.891	0.795	0.934
Sips	b_S		3.19	9.95	5.68	9.89	6.28	10.7	6.29	9.45	6.74
	n_S		1.11	0.768	1.24	0.816	1.22	0.839	1.27	0.909	1.31
	R^2		0.987	0.985	0.991	0.985	0.990	0.989	0.963	0.987	0.961
	AIC		-61	-54	-57	-53	-55	-55	-40	-53	-38
Temkin	a_T		54.7	79.3	252.0	99.9	286.6	125.3	356.4	145.7	475.8
	b_T		38.15	18.12	19.96	18.52	20.23	18.93	20.52	19.42	20.92
	R^2		0.981	0.946	0.960	0.946	0.954	0.947	0.945	0.946	0.938
	AIC		-65	-48	-47	-46	-46	-44	-43	-42	-40
Freundlich	k_F		0.254	0.582	0.676	0.619	0.703	0.657	0.744	0.682	0.790
	n_F		3.64	3.98	4.76	4.16	4.88	4.35	5.03	4.43	5.24
	R^2		0.966	0.906	0.951	0.910	0.947	0.915	0.921	0.918	0.921
	AIC		-63	-43	-47	-42	-55	-42	-40	-41	-39

Units: q_m : mmol Nd g⁻¹; b_L : L mmol⁻¹; b_S : (mmol L⁻¹)^{n_S}; k_F : mmol^{1-1/n_F} g⁻¹ L^{1/n_F}; a_T : L mmol⁻¹; b_T : J g mol⁻² × 10⁻⁶.

among the hard bases. The greater affinity of Nd(III) for A-PGMA and P-PGMA is consistent with the HSAB principle.

The Temkin equation gives also (in some cases) a good fit of experimental profiles. This model is usually associated with a linear decrease of the sorption heat with progressive saturation of the surface (by opposition to the Freundlich equation that considers that sorption heat varies logarithmically) [75,76]. The b_T coefficient refers to the Temkin isotherm constant (which is correlated to the heat of sorption): N-PGMA requires higher energy (~38 J g mol⁻²) for binding neodymium than A-PGMA (~18) and P-PGMA (~20). On the other hand, the Temkin isotherm equilibrium constant increases according the sequence: N-PGMA (~55 L mmol⁻¹) << A-PGMA (~79) << P-PGMA (~252).

Table S3 compares the sorption properties of the sorbents with those of other commercial or in-development materials (including commercial resins, inorganic sorbents, extractant impregnated supports, biosorbents, composite and magnetic-based materials). The most efficient sorbents consist of extractant impregnated alginate beads with highest sorption capacities ($q_{m,L}$) ~ 1.5 mmol Nd g⁻¹ [77], *Chlorella vulgaris* (~ 1.31 mmol Nd g⁻¹, [78]), or Jordanian diatomaceous earth (~ 1.18 mmol Nd g⁻¹, [79]). However, A-PGMA and P-PGMA show promising performances against alternative sorbents, while taking into account the equilibrium time, the affinity coefficient and the operative pH; these performances are comparable with those reported for activated charcoal [80] or *Sargassum* sp. [81].

3.2.3.2. Effect of temperature on sorption isotherms – Thermodynamic parameters. Temperature effects on sorption performance were studied in the range of 26–55 °C, using both A-PGMA and P-PGMA. Fig. 5 shows that both the sorption capacity and the coefficient of affinity (which is connected to the initial slope) for the two sorbents increase with increasing temperature: endothermic neodymium sorption.

Solid lines shows Langmuir fits (Sips fits are reported in Fig. S9). The Langmuir affinity coefficients (b_L) have been used for evaluating the thermodynamic parameters through the application of the van't Hoff equation. According to Lima et al. [82] the affinity coefficient was modified (i.e., b_L^*) to take into account the dimensionless criterion. Sorption capacity was expressed in molar units and affinity coefficient in using L mol⁻¹ unit and after correcting with:

$$b_L^* = b_L \frac{C_{adsorbate}^0}{\gamma_{adsorbate}} \quad (5)$$

where $C_{adsorbate}^0$ is the adsorbate unitary standard concentration (~1 mol L⁻¹) and $\gamma_{adsorbate}$ is the adsorbate activity coefficient

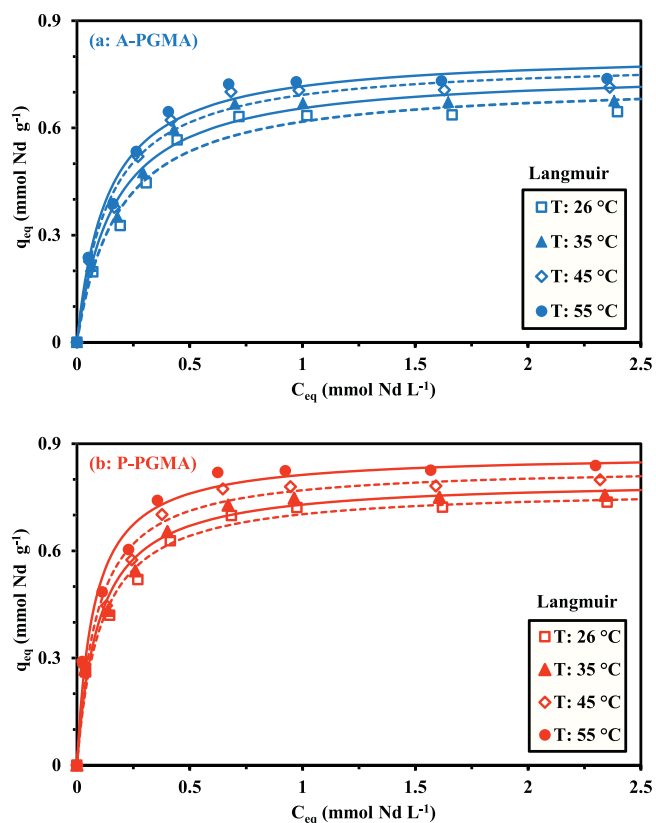


Fig. 5. Nd(III) sorption isotherms using A-PGMA (a) and P-PGMA (b) at pH₀ 4.5 at increasing temperatures – Using the Langmuir equation to model (C_0 : 0.17–0.72 mmol Nd L⁻¹; pH₀: 4.5; SD: 0.5 g L⁻¹; T: 26 ± 1 °C; time: 4 h; v: 200 rpm).

(dimensionless, and ~1 for dilute solutions).

$$\ln b_L^* = \frac{\Delta S^\circ}{R} - \frac{\Delta H^\circ}{R \times T} \quad (6)$$

$$\Delta G^\circ = \Delta H^\circ - T \Delta S^\circ \quad (7)$$

where ΔH° is the enthalpy change (kJ mol⁻¹), ΔG° is the change in Gibbs energy (kJ mol⁻¹) and ΔS° is the entropy change (J mol⁻¹ K⁻¹), R the

universal gas constant ($8.314 \text{ J mol}^{-1} \text{ K}^{-1}$).

Fig. S10 shows the Van't Hoff plots for both A-PGMA and P-PGMA sorbents. From the slope and intercept analysis it is possible determining the values of enthalpy and entropy changes (Table S4). The values are very close for A-PGMA and P-PGMA: 9.08 and 9.50 kJ mol^{-1} , for ΔH° , respectively, as well 54.0 and $56.3 \text{ J mol}^{-1} \text{ K}^{-1}$ for ΔS° . The positive values of the enthalpy change and entropy change clearly confirm endothermicity of sorption process and sorption enhances the randomness of the global system. The relatively low values of the enthalpy change also mean that the sorption of Nd(III) is highly effective requiring limited energy. Briao et al. [83] reported that Nd(III) sorption onto expanded vermiculite is exothermic (with a enthalpy change close to -20 kJ mol^{-1}). On the opposite hand, Javadian et al. [84] commented that the sorption of Nd(III) onto a magnetic alginate composite (bearing pyrimidine-thiophene-amide) is also endothermic and the enthalpy change ($\sim 13.7 \text{ kJ mol}^{-1}$) was of the same order as the values obtained with A-PGMA and P-PGMA. The negative value of the Gibbs energy change (-7 to -9 kJ mol^{-1}) means that the reaction is spontaneous, as a proof of the sorption process feasibility and favorability. As expected, the sorption process becomes more favorable with increasing the temperature. The favorability can be also assessed using the R_L coefficient (dimensionless):

$$R_L = \frac{1}{1 + b_L \times C_0} \quad (8)$$

where C_0 is the initial concentration of the solute (mmol L^{-1}). The sorption is favorable when $R_L < 1$. As expected, the R_L values decrease with increasing metal concentration: the sorption is favored with higher metal content in the aqueous phase and with increasing the temperature. For A-PGMA, the R_L values decrease from 0.52 to 0.05 . The sorption is even more favorable with P-PGMA: R_L values decrease from 0.38 to 0.03 .

The absolute value of $|T \times \Delta S^\circ|$ being systematically higher than $|\Delta G^\circ|$, it is generally accepted that the sorption is controlled by entropy change rather than enthalpy change.

The Clausius-Clapeyron equation was used to evaluate the isosteric heat of sorption (ΔH_x , kJ mol^{-1}) for different Nd(III) loadings (in the range q_{eq} : 0.1 - 0.6 / $0.7 \text{ mmol Nd g}^{-1}$, with corresponding C_{eq} values calculated from the Langmuir fits of sorption isotherms, at different temperatures) [85]:

$$-\frac{\Delta H_x}{R \times T^2} = \frac{d \ln C_{eq}}{d T} \quad (9)$$

or

$$\ln C_{eq} = \frac{\Delta H_x}{R} \times \frac{1}{T} + K_x \quad (10)$$

Fig. S11 shows the Clausius-Clapeyron plots for both A-PGMA and P-PGMA, while Table S5 reports the values of the isosteric heat of sorption at different metal loadings. The value of ΔH_x increases with Nd(III) content between 12.5 and 22.7 kJ mol^{-1} for A-PGMA and between 13.5 and 33.0 kJ mol^{-1} in the case of P-PGMA (Fig. S12). These positive values confirm the endothermic character of Nd(III) sorption on functionalized sorbents [86]. The order of magnitude (much lower than 80 kJ mol^{-1}) suggests that neodymium binding proceeds through physical sorption [85]. Lopicic et al. [87] reported that the increase of the isosteric heat of sorption with sorbent coverage can be associated with heterogeneous surface and/or lateral interactions between sorbed molecules (herein in contradiction with the poor fit of experimental sorption isotherms with the Freundlich equation). This increase is especially important when the sorption capacity exceeds $0.4 \text{ mmol Nd g}^{-1}$; while approaching the saturation of the sorbent, the heat of sorption sharply increases.

3.2.4. Sorbent reusability

The elution of Nd(III) from metal-loaded resins was performed with acidic solutions (0.5 M concentrations). Indeed, the affinity of the metal for the sorbent was strongly reduced in acidic solutions (cf. Section 3.2.1. on the pH effect), meaning that acidic solution may be highly efficient for reversing the sorption equilibrium. The type of acid strongly influences the efficiency of metal release. On both A-PGMA and P-PGMA, the eluents can be ranked according HNO_3 (~ 98 - 96%) $>$ HCl (~ 96 - 94%) $>$ H_2SO_4 (~ 78 - 71%) (Table S6). The preference for HCl and HNO_3 may be explained by the affinity of the rare earth for these ions (chloride or nitrate anions) compared with sulfuric acid (sulfate anion), and the solubility of relevant complexes. It is noteworthy that the desorption for Nd(III) from A-PGMA was more efficient than for P-PGMA. This result is consistent with the little higher strength of the complexes between Nd(III) and phosphonate-based ligands (compared with carboxylate-based moieties), as shown by thermodynamic parameters and affinity coefficients.

To test the recycling of the sorbents, nitric acid solutions (0.5 M) were used for five sorption/desorption consecutive cycles (See Table 3). The sorption efficiency declines progressively by 7% for A-PGMA and 9% for P-PGMA during the fifth cycle. For desorption, the efficiency decreases from 98 to 96% to 92 - 90% , respectively at the last step. The loss in sorption performance is roughly correlated to the decrease in desorption efficiency: the incomplete release of Nd(III) from the sorbents probably contributes to block sorption sites and quantitatively reduce the density of available reactive sites. However, it is noticeable that: by the 5th cycle, both sorbents had a sorption and desorption efficiencies of above 90% . The sorbents are stable in terms of global performance. The performance decay is comparable to the observations reported by Javadian et al. [84].

3.3. Application to leachate of monazite ore

Table S7 reports the analysis of REEs during the processing of the REE cake: concentrations in the pregnant liquor, the sorption capacities, the distribution ratio and the selectivity coefficient (using Yb as the reference for scaling, due to lower sorption levels) and the enrichment factor.

$$SC_{Metal/Yb} = \frac{D_{metal}}{D_{Yb}} = \frac{q_{m,metal} \times C_{eq,Yb}}{C_{eq,metal} \times q_{m,Yb}} \quad (11)$$

$$EF_{Metal} = \frac{C_{eq,metal}}{C_{0,metal}} \quad (12)$$

The total concentration of REEs in the pregnant solution reaches up to 10.4 mmol L^{-1} . The series of lanthanides can be divided based on atomic number into the "cerium group" (or "light" RE elements: from La to Gd), and the "yttrium group" (or "heavy" RE elements: Y, and from Tb to Lu) [88,89]. The LREEs represent about 78.2% of total REEs; this is consistent with their relative richness in Egyptian monazite. The cumulative sorption capacities reach 0.842 and $0.788 \text{ mmol g}^{-1}$ for A-PGMA and P-PGMA, where 91.9% and 87.8% are constituted of LREEs.

Table 3

Recycling of sorbents for Nd(III) sorption using A-PGMA and P-PGMA: sorption (SE) and desorption (DE) efficiencies (%).

Cycle #	A-PGMA		P-PGMA	
	SE (%)	DE (%)	SE (%)	DE (%)
1	100*	97.8	100*	96.4
2	96.9	96.6	97.3	95.3
3	95.9	95.6	95.4	94.2
4	94.5	92.7	93.0	91.9
5	93.1	91.9	91.0	90.3

(pH₀: 4.47; C₀: $0.706 \text{ mmol Nd L}^{-1}$; T: 26°C ; SD: 0.5 g L^{-1} – Desorption: 0.5 M HNO_3 ; SD: 1 g L^{-1} ; T: 26°C ; time: 90 min).

The sorbents little enrich the LREEs after the sorption step. This is confirmed in Fig. 6. It is noteworthy that A-PGMA shows little better performances for LREEs than P-PGMA with the notorious exception of Nd for which P-PGMA shows higher affinity (at least in terms of q_{eq} and D values). For HREEs, the two sorbents show comparable sorption performances. These cumulative sorption capacities exceed (by 15%) the maximum sorption capacities obtained for Nd(III) in synthetic solutions for A-PGMA. Surprisingly, for P-PGMA the trend is reversed; indeed, the cumulative sorption capacity decreases by 4% compared with Nd sorption (saturation level) from synthetic pure solutions. This may be associated with a difference in reactivity toward other metal ions present in the pre-treated leachate (heavy metal ions, for example) that may be more reactive onto phosphonic moieties, which, in turn, may limit their availability for Nd and other REEs.

In an attempt to correlate these trends in sorption properties to physicochemical properties of the members of REE family, the principles of QSAR (quantitative structure activity relationship, [90]) were applied considering some critical criteria such as: atomic number (AN), hydrated ionic radius (r , Å), Pauling electronegativity (X_m), covalent index ($X_m^2 r$), cation polarizing power (Z/r^2) (Table S8). Best correlations were obtained while plotting the distribution ratio vs. either AN or Z/r^2 (Fig. S13). It is noteworthy that the correlations are significantly better for A-PGMA sorbent (R^2 : 0.857 and 0.889, respectively, as shown by the plots in Fig. S13 a&c) than for P-PGMA. Indeed, in the case of P-PGMA, many irregularities are detected: more specifically the high efficiency of

the sorbent for Nd(III) leads to values of the distribution ratio that are much higher than predicted by the general trend. P-PGMA has a notorious affinity for Nd(III), meaning also that the binding involves different mechanisms than in the case of A-PGMA. In the case of the plots of D vs. AN, yttrium shows a distinct behavior, regarding its low AN (i.e., 39 vs. 57–70). However, considering the physicochemical properties of Y(III) (i.e., both hydrated ionic radius and electronegativity), yttrium is very close to dysprosium and holmium; the “equivalent” AN would be between 66 and 67. With this “equivalent” AN, the shift of Y point allows aligning this point to the general trend. The global trend associating sorption performance with cation polarizing power means that the ionic interaction is more representative than covalent binding (correlation with covalent index, where the plot of D vs. $X_m^2 r$ did not show clear trend, not shown).

3.4. Interpretation of sorption mechanisms

Based on the computational modeling (DFT and Theoretical vibrational spectra) and the information provided by the study of pH effect and FTIR characterization allow suggesting the interaction modes summarized in Scheme 2. Chelation and complexation mechanisms of Nd(III), with different heteroatoms (O and N) on the surface of the sorbents via different functional groups (such as $-OH$, $C(O)O-$, $C=O$, $P=O$, $P-OH$, $>N$ groups). For each sorbent, rises the possibility to bind Nd(III) (as $Nd(OH)_2^+$, $NdCl_2^+$, or $Nd(III)$) as four-membered or five-

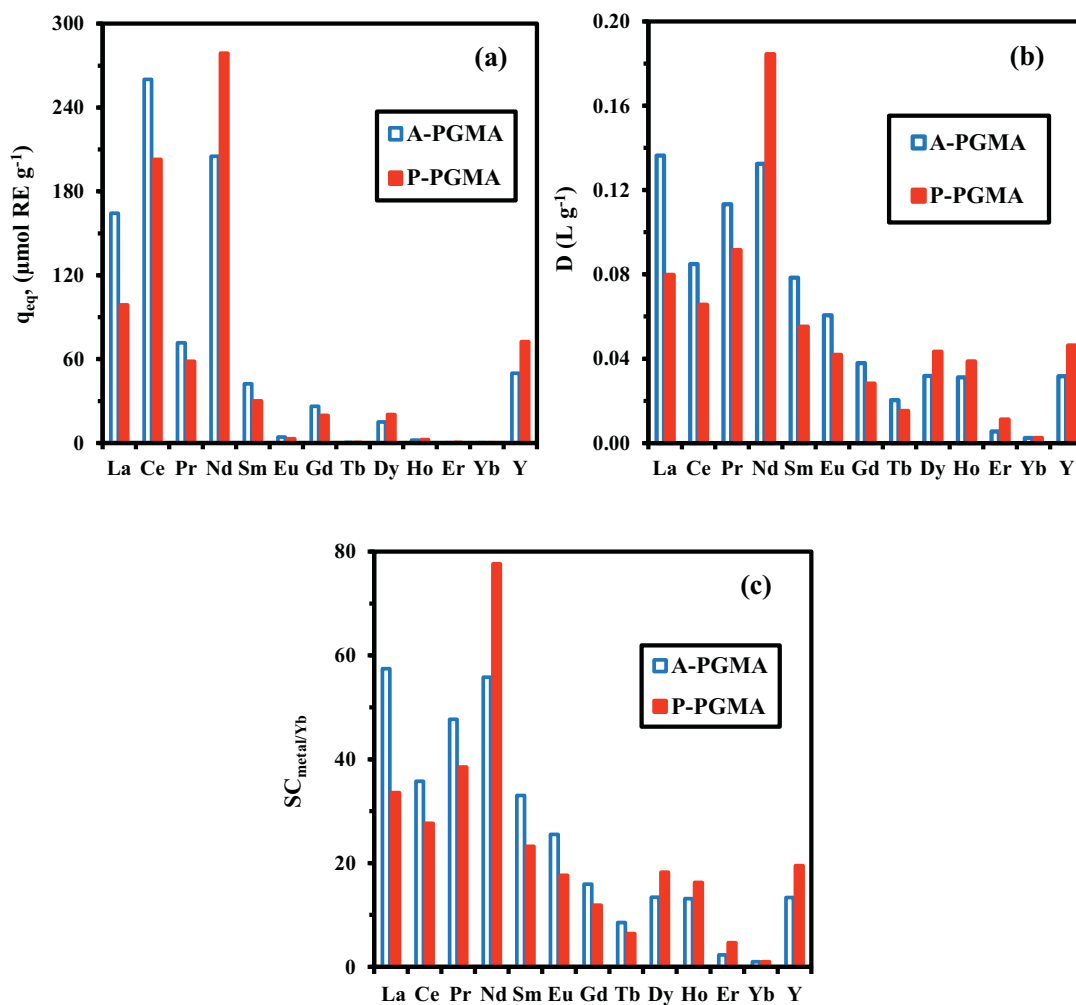
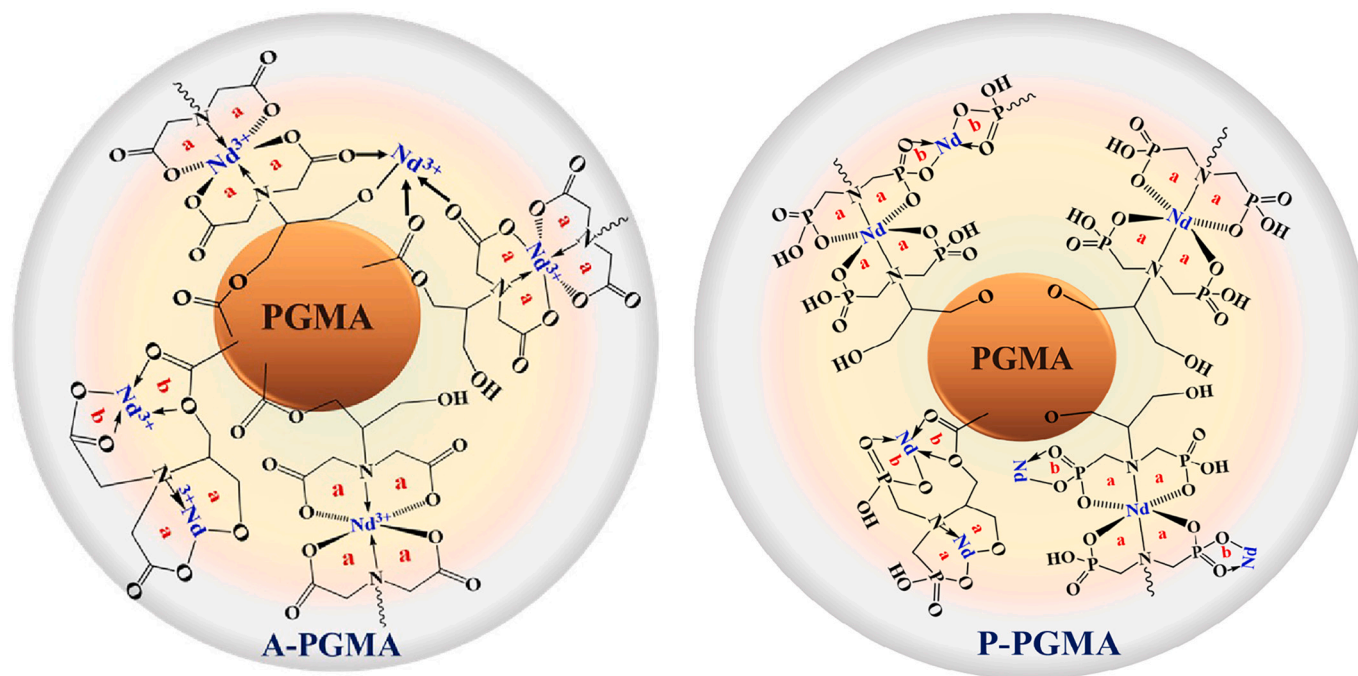


Fig. 6. Sorption tests for the recovery of REEs from pre-treated monazite leachate: (a) sorption capacities, (b) distribution ratio, and (c) $SC_{\text{metal/Yb}}$ (pH_0 : 4.02; SD: 0.5 $g L^{-1}$; time: 120 min; v: 200 rpm; T: 55 ± 1 °C).



Scheme 2. Tentative mechanisms involved in Nd(III) sorption using A-PGMA and P-PGMA (in individual schemes: a,b show five and four membered ring interaction modes, respectively).

membered complexes with carboxylate, amine groups and phosphonate moieties.

Furthermore, for the interacting of Nd(III) ions with two sorbent molecules/chains as shown in the Scheme 2 (i.e. the contribution modes a and b) forming two and/or four (five-membered chelating rings) and two (four-membered chelating rings); increasing the number of chelate rings; increases the stability of complex formed; which in turn, increase the metal sorption capacity.

3.4.1. FTIR characterization

FTIR spectroscopy was also used for characterizing the interaction modes and more specifically identifying the reactive groups affected by the binding of Nd(III) cations (Figs. S14 and S15, for full and selected wavenumber ranges, respectively). The appearance and disappearance of typical bands in the transmittance spectra, but also the shifts of some typical bands may characterize these modifications. For the two sorbents, the broad band (overlapped bands for -OH and -NH stretching vibrations) are little shifted.

For A-PGMA, after Nd(III) binding, the spectrum resembles that of sorbent: the bands intensity tends to decrease and red-shift at 3436 cm^{-1} and 2937 cm^{-1} (assigned to $-\text{CH}_2$ groups) moved to 3426 cm^{-1} and 2928 cm^{-1} , respectively. These alterations and changes are directly related to metal ion binding, that changes the -OH and -NH groups surroundings (bands superimposition that are not well-resolved).

For A-PGMA, the main significant changes are observed within the range of wavenumber: $1655\text{--}1500\text{ cm}^{-1}$:

(a) the band at 1721 cm^{-1} is blue shifted to 1726 cm^{-1} – the $\text{C}=\text{O}$ stretching vibration is affected by metal sorption;

(b) the band at 1631 cm^{-1} is blue shifted to 1636 cm^{-1} – neodymium forms a $\text{Nd}-\text{O}$ bond (through metal complexation with carboxylate groups);

(c) the bands at 1457 cm^{-1} , 1399 cm^{-1} , 1159 cm^{-1} (attributable to $\text{N}-\text{H}$ vibrations in secondary amines) moved to 1463 cm^{-1} , 1394 cm^{-1} and 1157 cm^{-1} – these changes are associated with $\text{Nd}-\text{N}$ bond of $\text{N}-\text{H}$ vibrations (in secondary amine).

For P-PGMA, the comparison of the spectra before and after metal sorption shows limited variations. The band at 1727 cm^{-1} ($\text{C}=\text{O}$

stretching) is not significantly affected by Nd(III) sorption (shift $\sim 1\text{ cm}^{-1}$). The relative intensity of the band at 1648 cm^{-1} increases; the band being red shifted to 1640 cm^{-1} . A strong band is observed at 1392 cm^{-1} ; this is usually a region where symmetric stretching of $\text{C}-\text{O}$ in hydroxyl groups [25] and $\text{C}-\text{N}$ stretch vibration in amine groups are observed [36]. The band observed at 1268 cm^{-1} (asymmetric $\text{P}=\text{O}$ stretching) is red-shifted to 1264 cm^{-1} , 1163 cm^{-1} ($\text{P}=\text{O}$) moved to 1161 cm^{-1} with a strong increase in intensity after neodymium binding. The bands at 740 cm^{-1} , 1463 cm^{-1} , 1627 cm^{-1} were blue-shifted to 750 cm^{-1} , 1469 cm^{-1} and 1638 cm^{-1} , respectively.

The FTIR spectrum revealed many bands corresponding to $\text{M}-\text{OH}$ vibrations and $\text{O}-\text{M}-\text{O}$ stretching at $400\text{--}800\text{ cm}^{-1}$ region [36]. After metal binding, the band at 503 cm^{-1} shifts ($\text{Nd}-\text{N}$ bond), the bands at 1068 cm^{-1} and 859 cm^{-1} ($\text{P}=\text{O}$ and $\text{P}=\text{OC}$ stretching bond) disappears and the $\text{M}-\text{O}$ bond appears at 633 cm^{-1} . Moreover, a new band related with the $\text{M}-\text{CO}$ bond may be seen between 530 cm^{-1} and 423 cm^{-1} [30]. Regardless, the chemical environment in which N- and P- reactive groups is influenced by Nd(III) binding.

In both sorbents, strong changes are seen in both sorbents for bands in the $400\text{--}800\text{ cm}^{-1}$ region, which is equivalent to $\text{M}-\text{OH}$ vibrations and $\text{O}-\text{M}-\text{O}$ stretching [30]. A new peak also appears at $420\text{--}423\text{ cm}^{-1}$ (usually related to the $\text{M}-\text{O}$ bond formation) [25,36].

The sorbents were tested and analyzed after five cycles of sorption and desorption to examine how stable they were when exposed to various solutions (sorption at pH 4.5 and desorption in HNO_3 solutions (0.5 M)). Figs. S14 and S15 indicate that the desorption stage partly recovers the sorbents FTIR spectra. It is noteworthy that, many tracer bands related to some sorbed metal ions were remained on the FTIR spectra of the regenerated sorbents after elution step, which can be consider as “intermediary” spectra between raw and metal-loaded sorbents.

For example, in the case of P-PGMA at the 2936 cm^{-1} , 1389 cm^{-1} or $750\text{--}400\text{ cm}^{-1}$ regions, the spectrum has not been completely recovered. Several other bands are altered (or at least not restored as in the spectrum of original material); showing that desorption is unable to return the spectrum to its original state. This is specifically observed for the regions:

(a) 1635–1589 cm^{-1} and 1454–1398 cm^{-1} (assigned to carboxylic/ carboxylate groups and amino groups, respectively [32]), and.

(b) 1000–850 cm^{-1} (P–C bonds) and 750–400 cm^{-1} .

3.4.2. DFT modeling.

Fig. 7 (top) illustrates the optimized structures of A-PGMA and P-PGMA; the chain to the support terminated by hydrogen is indicated by the green circle. To align with the optimal experimental conditions of pH = 4.5–5.0, acetate and phosphonate groups were deprotonated. All calculations were carried by the M06-2 \times /def-TZVP method [45,47,48], in water medium using the SMD variation of the polarizable continuum model [52].

As illustrated in Fig. 7 (middle) and tabulated in Table S9, Nd^{3+} binds to $[\text{A-PGMA}]^{2-}$ through nitrogen, two acetate oxygen moieties and the OH chain end opposite to the support, thereby replacing the

hydrogen bond that is present in $[\text{A-PGMA}]^{2-}$. With $\Delta G = -132.6 \text{ kJ mol}^{-1}$, the coordination is spontaneous. Nd^{3+} binds to $[\text{P-PGMA}]^{2-}$ in an analogous way and with closely similar Gibbs energy. However, Mayer bond order analysis reveals subtle differences, namely weakening of the Nd–N bond accompanied with strengthening of the Nd–O bonds in case of $[\text{P-PGMA}]^{2-}$. It is noteworthy that the binding of Nd^{3+} on $[\text{P-PGMA}]^{2-}$ is markedly different in gas-phase, where the phosphonate oxygen atoms coordinate to Nd, creating a seven-fold coordination environment. There is no corresponding structural change in case of $[\text{A-PGMA}]^{2-}$ when moving from gas-phase to water.

For comparison, Fig. 7 (bottom) illustrates analogous coordination of neutral NdCl_3 , where the Gibbs energy decreases by 50–60 kJ mol^{-1} , but remains exergonic. In this case, the order of strength is reversed in favor of $[\text{P-PGMA}]^{2-}$. In the case of $[\text{A-PGMA}]^{2-}$, changing Nd^{3+} to NdCl_3 slightly weakens both Nd–O and Nd–N bonds, in contrast to [P-

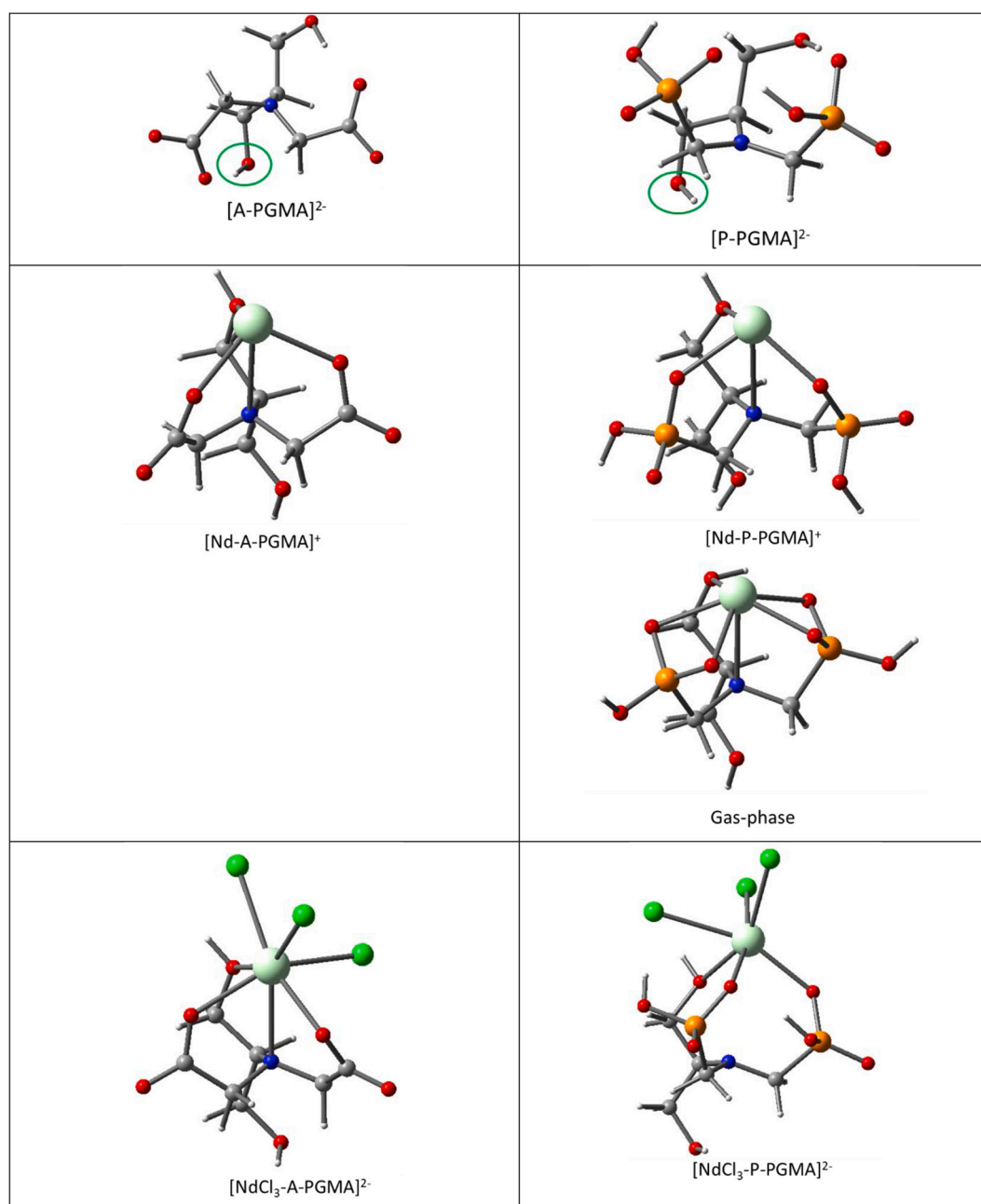


Fig. 7. Optimized structures of the studied acetate-PGMA and phosphonate-PGMA sorbents (Top), after Nd^{3+} complexation (Middle), and after NdCl_3 binding (Bottom) (in water medium).

PGMA]²⁻, where the weak Nd—N bond is (in practice) broken.

3.4.3. Theoretical vibrational spectra

The calculated vibrational spectra of [A-PGMA]²⁻ and [Nd-A-PGMA]²⁻ are compared in Fig. 8, focusing on wavenumbers relevant for the site of interaction. The dominant peaks arise from asymmetric C=O stretching modes of COO⁻, which blue-shift upon Nd sorption, while the corresponding symmetric stretching modes, at ca. 200 cm⁻¹ lower wavenumber, remain little affected. Another major effect of Nd sorption arises from replacement of hydrogen bonding of the OH-group, resulting in disappearance of the highest energy O—H deformation and redshift of a pair of lower energy O—H deformations.

4. Conclusion

The amination of poly(glycidyl) methacrylate allows preparing resin supports that can be readily functionalized by grafting either iminoacetic acid (A-PGMA) or iminophosphonate (P-PGMA) moieties onto PGMA. The chemical modifications are confirmed by titration, elemental analysis and FTIR analysis. FTIR characterization is also used, together with DFT modeling, for analyzing the mechanisms involved in neodymium binding: acetate groups are involved in A-PGMA and O donors from phosphonic units in P-PGMA, while amine groups contribute to stabilize metal binding.

The functionalization allows doubling the maximum values for Nd (III) sorption capacity. The sorption isotherms are fitted by the Langmuir equation and Nd(III) sorption process is endothermic, spontaneous and followed by the increased randomness of the system. The equilibrium is reached within 180–360 min; meaning that the resistance to intraparticle diffusion cannot be neglected. The kinetics profiles can be efficiently fitted by the pseudo-first order rate equation. Neodymium desorption (using 0.5 M HNO₃ solutions) is highly efficient and the sorbent can be recycled for at least five cycles. At the fifth cycle, the loss in sorption and desorption efficiencies approaches 9%; this is partly due to the progressive saturation of sorption sites (incomplete desorption) and some chemical modifications of the sorbents (confirmed by FTIR analysis).

The alkaline leaching of Egyptian monazite ore (rich in light REEs) generates effluents that were used for testing neodymium recovery from complex solutions. QSAR tools were used for correlating intrinsic properties of REEs with their relative affinity for A-PGMA and P-PGMA. The best correlations are obtained when plotting the distribution coefficients vs. either the atomic number (AN) or the cation polarizing power (i.e., Z²/r). However, iminophosphonate derivative (P-PGMA) has marked preference for Nd(III) (which is standing out of the linear regressions for other REEs).

CRedit authorship contribution statement

Ahmed A. Galhoum: Methodology, Investigation, Validation, Writing – original draft. **Takaya Akashi:** Conceptualization, Resources, Funding acquisition. **Mikko Linnolahti:** Investigation, Visualization, Writing – original draft. **Janne T. Hirvi:** Investigation, Visualization, Writing – original draft. **Abdullah G. Al-Sehemi:** Conceptualization, Visualization, Formal analysis, Data curation, Funding acquisition, Writing – review & editing. **Abul Kalam:** Conceptualization, Visualization, Formal analysis, Data curation, Funding acquisition, Writing – review & editing. **Eric Guibal:** Supervision, Software, Formal analysis, Data curation, Writing – review & editing.

Declaration of Competing Interest

The authors declare that they have no known competing financial interests or personal relationships that could have appeared to influence the work reported in this paper.

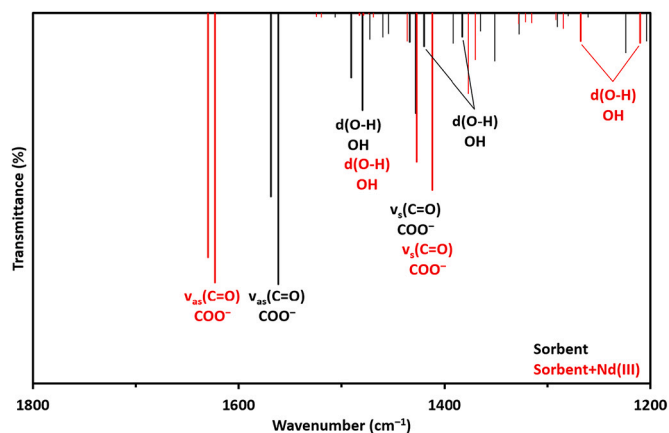


Fig. 8. Calculated vibrational spectra of [A-PGMA]²⁻ and [Nd-A-PGMA]²⁻ with identification of the relevant normal modes.

Data availability

No data was used for the research described in the article.

Acknowledgements

Authors acknowledge Hosei International Foundation, Japan (HIF-2017) and Nuclear Materials Authority (Egypt) for their support. Authors acknowledge support and funding of King Khalid University through Research Center for Advanced Materials Science (RCAMS) under grant no: RCAMS/KKU/0010/21. Special dedication to the memory of Prof. Dr. Ahmed Donia.

Appendix A. Supplementary data

Supplementary data to this article can be found online at <https://doi.org/10.1016/j.reactfunctpolym.2022.105389>.

References

- [1] V. Balaram, Rare earth elements: a review of applications, occurrence, exploration, analysis, recycling, and environmental impact, *Geosci. Front.* 10 (2019) 1285–1303.
- [2] L. Omodara, S. Pitkaaho, E.-M. Turpeinen, P. Saavalainen, K. Oravissjarvi, R. L. Keiski, Recycling and substitution of light rare earth elements, cerium, lanthanum, neodymium, and praseodymium from end-of-life applications - a review, *J. Clean. Prod.* 236 (2019), 117573.
- [3] S. Costis, K.K. Mueller, L. Coudert, C.M. Neculita, N. Reynier, J.F. Blais, Recovery potential of rare earth elements from mining and industrial residues: a review and cases studies, *J. Geochem. Explor.* 221 (2021), 106699.
- [4] A. Akcil, Y.A. Ibrahim, P. Meshram, S. Panda, Abhilashb, hydrometallurgical recycling strategies for recovery of rare earth elements from consumer electronic scraps: a review, *J. Chem. Technol. Biotechnol.* 96 (2021) 1785–1797.
- [5] R.Z. Rebello, M.T.W. Dias Carneiro Lima, L.H. Yamane, R.R. Siman, Characterization of end-of-life LED lamps for the recovery of precious metals and rare earth elements, *Resour. Conserv. Recycl.* 153 (2020), 104557.
- [6] S. Pavon, A. Fortuny, M.T. Call, A.M. Sastre, Improved rare earth elements recovery from fluorescent lamp wastes applying supported liquid membranes to the leaching solutions, *Sep. Purif. Technol.* 224 (2019) 332–339.
- [7] A.A. Maurice, K.N. Dinh, N.M. Charpentier, A. Brambilla, J.-C.P. Gabriel, Dismantling of printed circuit boards enabling electronic components sorting and their subsequent treatment open improved elemental sustainability opportunities, *Sustainability* 13 (2021).
- [8] D. Xia, N.M. Charpentier, A.A. Maurice, A. Brambilla, Q. Yan, J.-C.P. Gabriel, Sustainable route for Nd recycling from waste electronic components featured with unique element-specific sorting enabling simplified hydrometallurgy, *Chem. Eng. J.* 441 (2022), 135886.
- [9] H. Matsunaga, A.A. Ismail, Y. Wakui, T. Yokoyama, Extraction of rare earth elements with 2-ethylhexyl hydrogen 2-ethylhexyl phosphonate impregnated resins having different morphology and reagent content, *React. Funct. Polym.* 49 (2001) 189–195.
- [10] R.D. Abreu, C.A. Morais, Study on separation of heavy rare earth elements by solvent extraction with organophosphorus acids and amine reagents, *Miner. Eng.* 61 (2014) 82–87.

- [11] D. Kim, L. Powell, L.H. Delmau, E.S. Peterson, J. Herchenroeder, R.R. Bhawe, A supported liquid membrane system for the selective recovery of rare earth elements from neodymium-based permanent magnets, *Sep. Sci. Technol.* 51 (2016) 1716–1726.
- [12] X. Huang, J. Dong, L. Wang, Z. Feng, Q. Xue, X. Meng, Selective recovery of rare earth elements from ion-adsorption rare earth element ores by stepwise extraction with HEH(EHP) and HDEHP, *Green Chem.* 19 (2017) 1345–1352.
- [13] S. Inan, H. Tel, S. Sert, B. Cetinkaya, S. Sengul, B. Ozkan, Y. Altas, Extraction and separation studies of rare earth elements using Cyanex 272 impregnated Amberlite XAD-7 resin, *Hydrometallurgy* 181 (2018) 156–163.
- [14] N.N. Hidayah, S.Z. Abidin, The evolution of mineral processing in extraction of rare earth elements using liquid-liquid extraction: a review, *Miner. Eng.* 121 (2018) 146–157.
- [15] A.C. Ni'am, Y.-F. Wang, S.-W. Chen, G.-M. Chang, S.-J. You, Simultaneous recovery of rare earth elements from waste permanent magnets (WPMs) leach liquor by solvent extraction and hollow fiber supported liquid membrane, *Chem. Eng. Process. Process Intensif.* 148 (2020), 107831.
- [16] X. Heres, V. Blet, P. Di Natale, A. Ouaattou, H. Mazouz, D. Dhiba, F. Cuer, Selective extraction of rare earth elements from phosphoric acid by ion exchange resins, *Metals* 8 (2018) 8090682.
- [17] V.N. Rychkov, E.V. Kirillov, S.V. Kirillov, G.M. Bunkov, M.A. Mashkovtsev, M. S. Botalov, V.S. Semenishchev, V.A. Volkovich, Selective ion exchange recovery of rare earth elements from uranium mining solutions, in: A.A. Rempel, V. A. Volkovich (Eds.), *Physics, Technologies and Innovation*, 2016.
- [18] J. Guo, J. Cai, Q. Su, Ion imprinted polymer particles of neodymium: synthesis, characterization and selective recognition, *J. Rare Earths* 27 (2009) 22–27.
- [19] K.L. Ang, D. Li, A.N. Nikoloski, The effectiveness of ion exchange resins in separating uranium and thorium from rare earth elements in acidic aqueous sulfate media. Part 2. Chelating resins, *Miner. Eng.* 123 (2018) 8–15.
- [20] D. Gomes Rodrigues, S. Monge, S.p. Pellet-Rostaing, N. Dacheux, D. Bouyer, C. Faur, Sorption properties of carbonylmethylphosphonated-based polymer combining both sorption and thermosensitive properties: new valuable hydro-soluble materials for rare earth elements sorption, *Chem. Eng. J.* 355 (2019) 871–880.
- [21] S. Virolainen, E. Repo, T. Sainio, Recovering rare earth elements from phosphogypsum using a resin-in-leach process: selection of resin, leaching agent, and eluent, *Hydrometallurgy* 189 (2019), 105125.
- [22] A.R. Elsalamouny, O.A. Desouky, S.A. Mohamed, A.A. Galhoum, E. Guibal, Evaluation of adsorption behavior for U(VI) and Nd(III) ions onto fumarated polystyrene microspheres, *J. Radioanal. Nucl. Chem.* 314 (2017) 429–437.
- [23] D. Kolodynska, D. Fila, Z. Hubicki, Evaluation of possible use of the macroporous ion exchanger in the adsorption process of rare earth elements and heavy metal ions from spent batteries solutions, *Chem. Eng. Process. Process Intensif.* 147 (2020), 107767.
- [24] D. Kolodynska, Z. Hubicki, D. Fila, Recovery of rare earth elements from acidic solutions using macroporous ion exchangers, *Sep. Sci. Technol.* 54 (2019) 2059–2076.
- [25] Y. Wei, K.A.M. Salih, K. Rabie, K.Z. Elwakeel, Y.E. Zayed, M.F. Hamza, E. Guibal, Development of phosphoryl-functionalized algal-PEI beads for the sorption of Nd (III) and Mo(VI) from aqueous solutions – application for rare earth recovery from acid leachates, *Chem. Eng. J.* 412 (2021), 127399.
- [26] D.L. Ramasamy, V. Puhakka, S. Iftekhara, A. Wojtus, E. Repo, S. Ben Hammouda, E. Iakovleva, M. Sillanpaa, N- and O- ligand doped mesoporous silica-chitosan hybrid beads for the efficient, sustainable and selective recovery of rare earth elements (REE) from acid mine drainage (AMD): understanding the significance of physical modification and conditioning of the polymer, *J. Hazard. Mater.* 348 (2018) 84–91.
- [27] H.-J. Park, L.L. Tavlarides, Adsorption of neodymium(III) from aqueous solutions using a phosphorus functionalized adsorbent, *Ind. Eng. Chem. Res.* 49 (2010) 12567–12575.
- [28] M.F. Hamza, K.A.M. Salih, A.A.H. Abdel-Rahman, Y.E. Zayed, Y. Wei, J. Liang, E. Guibal, Sulfonic-functionalized algal/PEI beads for scandium, cerium and holmium sorption from aqueous solutions (synthetic and industrial samples), *Chem. Eng. J.* 403 (2021), 126399.
- [29] S. Rangabhashiyam, K. Vijayaraghavan, Biosorption of tm(III) by free and polysulfone-immobilized *Turbinarina conoides* biomass, *J. Ind. Eng. Chem.* 80 (2019) 318–324.
- [30] S. Iftekhara, V. Srivastava, M. Sillanpaa, Synthesis and application of LDH intercalated cellulose nanocomposite for separation of rare earth elements (REEs), *Chem. Eng. J.* 309 (2017) 130–139.
- [31] A.A. Galhoum, M.G. Mahfouz, S.T. Abdel-Rehem, N.A. Gomaa, A.A. Atia, T. Vincent, E. Guibal, Diethylenetriamine-functionalized chitosan magnetic nano-based particles for the sorption of rare earth metal ions Nd(III), Dy(III) and Yb(III), *Cellulose* 22 (2015) 2589–2605.
- [32] A.A. Tolba, S.I. Mohamady, S.S. Hussin, T. Akashi, Y. Sakai, A.A. Galhoum, E. Guibal, Synthesis and characterization of poly(carboxymethyl)-cellulose for enhanced La(III) sorption, *Carbohydr. Polym.* 157 (2017) 1809–1820.
- [33] A.A. Galhoum, M.G. Mahfouz, S.T. Abdel-Rehem, N.A. Gomaa, A.A. Atia, T. Vincent, E. Guibal, Cysteine-functionalized chitosan magnetic nano-based particles for the recovery of light and heavy rare earth metals: uptake kinetics and sorption isotherms, *Nanomaterials* 5 (2015) 154–179.
- [34] E.A. Imam, I. El-Tantawy El-Sayed, M.G. Mahfouz, A.A. Tolba, T. Akashi, A. A. Galhoum, E. Guibal, Synthesis of α -aminophosphonate functionalized chitosan sorbents: effect of methyl vs phenyl group on uranium sorption, *Chem. Eng. J.* 352 (2018) 1022–1034.
- [35] X. Sun, L. Yang, H. Xing, J. Zhao, X. Li, Y. Huang, H. Liu, Synthesis of polyethylenimine-functionalized poly(glycidyl methacrylate) magnetic microspheres and their excellent Cr(VI) ion removal properties, *Chem. Eng. J.* 234 (2013) 338–345.
- [36] A.A. Galhoum, E.A. Elshehy, D.A. Tolan, A.M. El-Nahas, T. Taketsugu, K. Nishikiori, T. Akashi, A.S. Morshedy, E. Guibal, Synthesis of polyaminophosphonic acid-functionalized poly(glycidyl methacrylate) for the efficient sorption of La(III) and Y(III), *Chem. Eng. J.* 375 (2019), 121932.
- [37] M. Benaglia, A. Alberti, L. Giorgini, F. Magnoni, S. Tozzi, Poly(glycidyl methacrylate): a highly versatile polymeric building block for post-polymerization modifications, *Polym. Chem.* 4 (2013) 124–132.
- [38] A.A. Galhoum, Facile synthesis of functionalized polyglycidylmethacrylate-magnetic nanocomposites for enhanced uranium sorption, *RSC Adv.* 9 (2019) 38783–38796.
- [39] M.V. Lopez-Ramon, F. Stoeckli, C. Moreno-Castilla, F. Carrasco-Marin, On the characterization of acidic and basic surface sites on carbons by various techniques, *Carbon* 37 (1999) 1215–1221.
- [40] O.A. Desouky, Solvent extraction study on uranium and thorium from sulfuric acid solution and its technological application, in: *Chemistry Department, Zagazig University, Banha (Egypt)*, 1998.
- [41] A. Sroor, Passive and active measurements of Egyptian monazite samples, *Appl. Radiat. Isot.* 58 (2003) 281–285.
- [42] C.K. Gupta, N. Krishnamurthy, *Extractive Metallurgy of Rare Earths*, CRC Press, Boca Raton (FL), USA, 2005.
- [43] A.M. Abdel-Rehim, An innovative method for processing Egyptian monazite, *Hydrometallurgy* 67 (2002) 9–17.
- [44] C.A. Morais, J.S. Benedetto, V.S.T. Ciminelli, Recovery of cerium by oxidation/hydrolysis with $\text{KMnO}_4 - \text{Na}_2\text{CO}_3$, in: *electrometallurgy and environmental, Hydrometallurgy* (2003) 1773–1782.
- [45] Y. Zhao, D.G. Truhlar, The M06 suite of density functionals for main group thermochemistry, thermochemical kinetics, noncovalent interactions, excited states, and transition elements: two new functionals and systematic testing of four M06-class functionals and 12 other functionals, *Theor. Chem. Accounts* 120 (2008) 215–241.
- [46] A. Jaoul, G. Nocton, C. Clavaguera, Assessment of density functionals for computing thermodynamic properties of lanthanide complexes, *ChemPhysChem* 18 (2017) 2688–2696.
- [47] A. Schäfer, C. Huber, R. Ahlrichs, Fully optimized contracted Gaussian basis sets of triple zeta valence quality for atoms Li to Kr, *J. Chem. Phys.* 100 (1994) 5829–5835.
- [48] K. Eichkorn, F. Weigend, O. Treutler, R. Ahlrichs, Auxiliary basis sets for main row atoms and transition metals and their use to approximate coulomb potentials, *Theor. Chem. Accounts* 97 (1997) 119–124.
- [49] M. Dolg, H. Stoll, H. Preuss, Energy-adjusted ab initio pseudopotentials for the rare earth elements, *J. Chem. Phys.* 90 (1989) 1730–1734.
- [50] T. Lu, F. Chen, Multiwfn: a multifunctional wavefunction analyzer, *J. Comput. Chem.* 33 (2012) 580–592.
- [51] M.J. Frisch, G.W. Trucks, H.B. Schlegel, G.E. Scuseria, M.A. Robb, J.R. Cheeseman, G. Scalmani, V. Barone, G.A. Petersson, H. Nakatsuji, X. Li, M. Caricato, A. V. Marenich, J. Bloino, B.G. Janesko, R. Gomperts, B. Mennucci, H.P. Hratchian, J. V. Ortiz, A.F. Izmaylov, J.L. Sonnenberg, F. Ding Williams, F. Lipparini, F. Egidi, J. Goings, B. Peng, A. Petrone, T. Henderson, D. Ranasinghe, V.G. Zakrzewski, J. Gao, N. Rega, G. Zheng, W. Liang, M. Hada, M. Ehara, K. Toyota, R. Fukuda, J. Hasegawa, M. Ishida, T. Nakajima, Y. Honda, O. Kitao, H. Nakai, T. Vreven, K. Throssell, J.A. Montgomery Jr., J.E. Peralta, F. Ogliaro, M.J. Bearpark, J. J. Heyd, E.N. Brothers, K.N. Kudin, V.N. Staroverov, T.A. Keith, R. Kobayashi, J. Normand, K. Raghavachari, A.P. Rendell, J.C. Burant, S.S. Iyengar, J. Tomasi, M. Cossi, J.M. Millam, M. Klene, C. Adamo, R. Cammi, J.W. Ochterski, R.L. Martin, K. Morokuma, O. Farkas, J.B. Foresman, D.J. Fox, *Gaussian 16 Rev. C.01*, in, Wallingford, CT, 2016.
- [52] A.V. Marenich, C.J. Cramer, D.G. Truhlar, Universal solvation model based on solute electron density and on a continuum model of the solvent defined by the bulk dielectric constant and atomic surface tensions, *J. Phys. Chem. B* 113 (2009) 6378–6396.
- [53] R.C. Shier, J.L. Fulton, M. Balasubramanian, M.-T. Nguyen, J.-B. Lu, J. Li, R. Rousseau, V.-A. Glezakou, D.C. Cantu, Coordination sphere of lanthanide aqua ions resolved with ab initio molecular dynamics and X-ray absorption spectroscopy, *Inorg. Chem.* 60 (2021) 3117–3130.
- [54] L.D. Pachon, P. Gamez, J.J.M. van Brussel, J. Reedijk, Zinc-catalyzed aminolysis of epoxides, *Tetrahedron Lett.* 44 (2003) 6025–6027.
- [55] A.A. Galhoum, W.H. Eisa, I.E.-T. El-Sayed, A.A. Tolba, Z.M. Shalaby, S. I. Mohamady, S.S. Muhammad, S.S. Hussien, T. Akashi, E. Guibal, A new route for manufacturing poly(aminophosphonic)-functionalized poly(glycidyl methacrylate)-magnetic nanocomposite - application to uranium sorption from ore leachate, *Environ. Pollut.* 264 (2020), 114797.
- [56] C. Liu, R. Bai, L. Hong, T. Liu, Functionalization of adsorbent with different aliphatic polyamines for heavy metal ion removal: characteristics and performance, *J. Colloid Interface Sci.* 345 (2010) 454–460.
- [57] T. Caykara, F. Cakar, S. Demirci, A new type of poly(glycidyl methacrylate) microbeads with surface grafted iminodiacetic acid: synthesis and characterization, *Polym. Bull.* 61 (2008) 311–318.
- [58] B. Yu, B. Yang, G. Li, H. Cong, Preparation of monodisperse cross-linked poly(glycidyl methacrylate)/Fe₃O₄@diazo resin magnetic microspheres with dye removal property, *J. Mater. Sci.* 53 (2018) 6471–6481.

- [59] F.C. Wang, J.M. Zhao, W.K. Wang, Z.Z. Tong, Adsorption of Au(III) by amino-modified monodispersed PGMA microspheres and deposition of gold nanoparticles, *Rare Metals* 37 (2018) 196–203.
- [60] J. Zhao, S. Wang, L. Zhang, C. Wang, B. Zhang, Kinetic, isotherm, and thermodynamic studies for Ag(I) adsorption using carboxymethyl functionalized poly(glycidyl methacrylate), *Polymers* 10 (2018) 1090.
- [61] K. Riedelsberger, W. Jaeger, Polymeric aminomethylphosphonic acids - 1. Synthesis and properties in solution, *Des. Monomers Polym.* 1 (1998) 387–407.
- [62] C. Muthuselvi, S.S. Pandiarajan, B. Ravikumar, S. Athimoolam, N. Srinivasan, R. V. Krishnakumar, FT-IR and FT-Raman spectroscopic analyses of indeno quinoxaline derivative crystal, *Asian, J. Appl. Sci.* 11 (2018) 83–91.
- [63] Z. Zhou, F. Jiang, T.-C. Lee, T. Yue, Two-step preparation of nano-scaled magnetic chitosan particles using Triton X-100 reversed-phase water-in-oil microemulsion system, *J. Alloys Compd.* 581 (2013) 843–848.
- [64] S. Ko, J. Jang, Protein immobilization on aminated poly(glycidyl methacrylate) nanofibers as polymeric carriers, *Biomacromolecules* 8 (2007) 1400–1403.
- [65] R. Williams, pKa data (compiled by R. Williams), in, University of Wisconsin, Provided by the ACS, Organic Division (2017). http://www.chem.wisc.edu/area_s/reich/pkatable/pKa_compilation-1-Williams.pdf. (Accessed 4 June 2017).
- [66] M. Imperiyka, A. Ahmad, S.A. Hanifah, F. Bella, A UV-prepared linear polymer electrolyte membrane for dye-sensitized solar cells, *Physica B* 450 (2014) 151–154.
- [67] A.B. Hugues, Amino acids, peptides and proteins in organic chemistry, in: A. B. Hugues (Ed.), Volume 2 - Modified Amino Acids, Organocatalysis and Enzymes, Wiley-VCH, Weinheim (Germany), 2009, p. 683.
- [68] J.P. Gustafsson, Visual MINTEQ. <https://vminteq.lwr.kth.se/>, 2013. Accessed: April 2019, in, KTH, Royal Institute of Technology, Stockholm, Sweden.
- [69] M.A. Hubbe, S. Azizian, S. Douven, Implications of apparent pseudo-second-order adsorption kinetics onto cellulosic materials: a review, *BioResources* 14 (2019) 7582–7626.
- [70] J.-P. Simonin, On the comparison of pseudo-first order and pseudo-second order rate laws in the modeling of adsorption kinetics, *Chem. Eng. J.* 300 (2016) 254–263.
- [71] Y.S. Ho, G. McKay, Pseudo-second order model for sorption processes, *Process Biochem.* 34 (1999) 451–465.
- [72] J. Crank, *The Mathematics of Diffusion*, 2nd. ed., Oxford University Press, Oxford, U.K., 1975.
- [73] Y. Marcus, *Ion Properties*, Marcel Dekker, Inc., New York, NY, 1997.
- [74] R.G. Pearson, *Acids and Bases* vol. 151, Science (New York, N.Y., 1966, pp. 172–177.
- [75] Y.S. Ho, J.F. Porter, G. McKay, Equilibrium isotherm studies for the sorption of divalent metal ions onto peat: copper, nickel and lead single component systems, *Water Air Soil Pollut.* 141 (2002) 1–33.
- [76] M.A. Al-Ghouti, D.A. Da'ana, Guidelines for the use and interpretation of adsorption isotherm models: a review, *J. Hazard. Mater.* 393 (2020), 122383.
- [77] L. Zhang, D. Wu, B. Zhu, Y. Yang, L. Wang, Adsorption and selective separation of neodymium with magnetic alginate microcapsules containing the extractant 2-ethylhexyl phosphonic acid mono-2-ethylhexyl ester, *J. Chem. Eng. Data* 56 (2011) 2280–2289.
- [78] M.A. Kucuker, N. Wiczorek, K. Kuchta, N.K. Copt, Biosorption of neodymium on *Chlorella vulgaris* in aqueous solution obtained from hard disk drive magnets, *PLoS One* 12 (2017) 0175255.
- [79] I. Hamadneh, A. Alatawi, R. Zalloum, R. Albuqain, S. Alstari, F.I. Khalili, A.H. Al-Dujaili, Comparison of Jordanian and standard diatomaceous earth as an adsorbent for removal of Sm(III) and Nd(III) from aqueous solution, *Environ. Sci. Pollut. Res.* 26 (2019) 20969–20980.
- [80] R. Qadeer, Adsorption of neodymium ions on activated charcoal from aqueous solutions, *J. Radioanal. Nucl. Chem.* 265 (2005) 377–381.
- [81] R.C. Oliveira, O. Garcia Jr., Study of biosorption of rare earth metals (La, Nd, Eu, Gd) by *Sargassum* sp biomass in batch systems: Physicochemical evaluation of kinetics and adsorption models, in: E.R. Donati, M.R. Viera, E.L. Tavani, M. A. Giaveno, T.L. Lavalle, P.A. Chiacchiarini (Eds.), *Biohydrometallurgy: A Meeting Point between Microbial Ecology*, Trans Tech Publications, Switzerland, Metal Recovery Processes and Environmental Remediation, 2009, pp. 605–608.
- [82] E.C. Lima, A. Hosseini-Bandegharai, J.C. Moreno-Piraján, I. Anastopoulos, A critical review of the estimation of the thermodynamic parameters on adsorption equilibria. Wrong use of equilibrium constant in the Van't Hoff equation for calculation of thermodynamic parameters of adsorption, *J. Mol. Liq.* 273 (2019) 425–434.
- [83] G.d.V. Briao, M.G. Carlos da Silva, M.G. Adeodato Vieira, Neodymium recovery from aqueous solution through adsorption/desorption onto expanded vermiculite, *Appl. Clay Sci.* 198 (2020), 105825.
- [84] H. Javadian, M. Ruiz, M. Taghvaei, A.M. Sastre, Novel magnetic nanocomposite of calcium alginate carrying poly (pyrimidine-thiophene-amide) as a novel green synthesized polyamide for adsorption study of neodymium, terbium, and dysprosium rare-earth ions, *Colloids Surf. A Physicochem. Eng. Asp.* 603 (2020), 125252.
- [85] N. Guo, X. Lv, Q. Li, T. Ren, H. Song, Q. Yang, Removal of hexavalent chromium from aqueous solution by mesoporous α -FeOOH nanoparticles: performance and mechanism, *Microporous Mesoporous Mater.* 299 (2020), 110101.
- [86] N. Sivarajasekar, R. Baskar, Adsorption of basic Magenta II onto H₂SO₄ activated immature *Gossypium hirsutum* seeds: kinetics, isotherms, mass transfer, thermodynamics and process design, *Arab. J. Chem.* 12 (2019) 1322–1337.
- [87] Z.R. Lopicic, M.D. Stojanovic, T.S.K. Radoicic, J.V. Milojkovic, M.S. Petrovic, M. L. Mihajlovic, M.L.J. Kijevcanin, Optimization of the process of Cu(II) sorption by mechanically treated *Prunus persica* L. - contribution to sustainability in food processing industry, *J. Clean. Prod.* 156 (2017) 95–105.
- [88] N.N. Greenwood, A. Earnshaw, *Chemistry of the Elements*, 2nd. ed., Butterworth-Heinemann, Oxford, UK, 1997.
- [89] S. Cotton, *Lanthanide and Actinide Chemistry*, John Wiley & Sons, Ltd, Chichester, UK, 2006.
- [90] C. Chen, J. Wang, Correlating metal ionic characteristics with biosorption capacity using QSAR model, *Chemosphere* 69 (2007) 1610–1616.